IFS #195

Drift Modes with Differential Rotation and Passing Electrons

J. Liu, W. Horton, and J.E. Sedlak
Institute for Fusion Studies
The University of Texas at Austin
Austin, Texas 78712-1068

Abstract

Differential rotation characteristic of the tandem mirror central cell is shown to have a significant stabilizing effect on the rotation and unfavorable curvature driven drift modes. Stability boundaries and parametric dependence of the growth rate and frequency of the m=1 and m=2 modes are given as a function of the passing electron density fraction, wall-to-plasma radius and rotation speed.

I. Introduction

The low frequency fluctuations with low aximuthal mode numbers and rotating in the ion diamagnetic direction with speeds near the equilibrium $E \times B$ drift velocity are observed in numerous tandem mirror experiments and have attracted considerable attention. In Ref. 1 Horton and Liu suggest the possibility that the low m rotation driven drift modes may be responsible for the fluctuations. The conventional FLR-MHD, rigid rotor modes studied in Ref. 2 for the axisymmetric tandem mirror are stable at the low plasma pressure in the experiments where the modes are observed due to the magnetic energy required for bending the magnetic field. The flute-like drift modes called trapped particle modes by Rosenbluth[3] and Berk et al.[4] are driven unstable by the plasma pressure gradient acting across the unfavorably curved magnetic field in the transitional regions at the ends of the central cell and are another candidate for the observed low m oscillations.

In the present work we extend the rotationally driven drift mode model of Horton and Liu[1] to include the effects of the pasing electron population and the effect of differential rotation in the plasma equilibrium. The drift modes have frequencies greater than the ion transit frequency and less than the electron transit frequency over the length of the central cell. To keep the analysis simple, while anticipating the need for future nonlinear studies of the unstable system, a reduced hydrodynamic description of the system is used including the finite ion gyroradius fluid equations and two-component electron fluid equations.

The stability analysis is given first for the solid-body or rigidly rotating plasma which permits an analytic solution and secondly by using a shooting method eigenvalue code to determine the modes of general radial profiles with differential rotation. The eigenvalue analysis allows consideration of profiles which have free energy from both radial gradients and sheared rotation. We show that contrary to a simple free energy argument that a mildly sheared rotational flow is a substantial stabilizing effect. The stability arises from the fact that the interchange of plasma pressure from the inner high pressure region to the outer low pressure region is inhibited by the differential rotation in analogy with the well-known stabilizing effect of magnetic shear. The free energy in the sheared flow of differential rotation is released by a different kind of eigenfunction working on the radial mixing of the angular momentum gradient rather than the pressure gradient. Since the dy-

namics represented by the eigenfunctions of the pressure gradient and sheared flow modes are rather different, there are more stable plasma configurations with both monotonically decreasing density and rotational profiles.

In Sec. II we derive the reduced rotational drift mode equations including the finite Larmor radius stress tensor and passing electrons. In Sec. III we investigate the stability of solid-body rotation with a Gaussian density profile. We present formulas for the threshold and cut-off passing electron density ratio as a function of rotational speed, effective gravity, the wall radius, and the ion-to-electron temperature ratio. In Sec. IV we present the numerical study of stability with the shooting code. In Sec. V we present the summary and conclusions.

II. Trapped Electron Mode from Fluid Equations

In this section we use hydrodynamic equations with the finite ion gyro radius stress tensor in the ion fluid and a two-component electron fluid consisting of trapped and passing components to derive the equations for the trapped electron mode in a cylindrical model of the axisymmetric tandem mirror. The two-component electron fluid model has been used for trapped particle modes by Rosenbluth[3] for tandem mirrors. The analysis shows that this hydrodynamic description gives a good simplified description of the modes compared with that given by the Vlasov description used by Kesner and Lane.[5] The hydrodynamic description given here is valid for modes with frequencies greater than the ion-transit frequency and less than the electron transit frequency. We restrict consideration here to the electrostatic approximation.

A. Ion Hydrodynamic Equations

The finite Larmor radius fluid equations for the ions are the continuity equation

$$\frac{\partial n_i}{\partial t} + \nabla \cdot (n_i \mathbf{v}_i) = 0 \tag{1}$$

and the momentum-balance equation

$$m_i n_i \frac{d\mathbf{v}_i}{dt} + \nabla \cdot \overleftrightarrow{\pi} = e_i n_i \left(\mathbf{E} + \frac{\mathbf{v}_i}{c} \times \mathbf{B} \right) - T_i \nabla n_i + m_i n_i \mathbf{g} \tag{2}$$

where we use the constant ion temperature approximation to close the hierarchy of moment equations. The gravitational force is taken as $\mathbf{g} = -\nabla U$ where U includes the effects of rf ponderomotive forces and the magnetic curvature within the cylindrical model. In Eq. (2) $\overleftrightarrow{\pi}$ is the well-known finite Larmor radius stress tensor.

Solving Eq. (2) for the flux $n_i \mathbf{v}_i$ by expanding in $1/\omega_{ci}$ where $\omega_{ci} = e_i B/m_i c$ we obtain

$$n\mathbf{v}_i = \frac{c}{B}\hat{z} \times \nabla\phi + \frac{cT_i}{e_i B}\hat{z} \times \nabla n_i + \frac{c\hat{z}}{e_i B} \times \left(m_i n_i \frac{d\mathbf{v}_i}{dt} + \nabla \cdot \overleftrightarrow{\pi} \right) - \frac{cm_i n_i}{e_i B}\hat{z} \times \mathbf{g} \tag{3}$$

where the first two terms are of order $\varepsilon n_i v_{th,i}$ and the third and last terms are of order $\varepsilon^3 n_i v_{th,i}$ where $\varepsilon = v_{th,i}/a\omega_{ci} = \rho_i/a$ is the finite gyroradius expansion parameter. We may write the first order ion fluid velocity as

$$\mathbf{v}_i^{(1)} = \frac{c\hat{z} \times \nabla\psi}{B} \tag{4}$$

with the stream function ψ given by

$$\psi = \phi + \frac{T_i}{e_i} \ell n\, n_i.$$

By iteration we calculate the polarization drift and the finite Larmor radius stress tensor with $\mathbf{v}_i^{(1)}$ to obtain the nonlinear flux in Eq. (3) correct to third order in ε. We then compute the divergence of the flux and express the results in terms of the Poisson brackets defined by $[f,g] = \hat{z} \cdot \nabla f \times \nabla g$. After considerable algebra[6] we obtain the reduced nonlinear ion continuity equation

$$\frac{\partial n_i}{\partial t} + \frac{c}{B}[\phi, n_i] - \frac{c}{\omega_{ci} B} \nabla \cdot \left\{ n_i \frac{\partial}{\partial t} \nabla\phi + \frac{cn_i}{B}[\phi, \nabla\phi] + \frac{cT_i}{e_i B}[n_i, \nabla\phi] \right\} - \frac{1}{\omega_{ci}}[n_i, U] = 0. \tag{5}$$

We separate Eq. (6) into its mean and fluctuating components by writing

$$\begin{aligned}\phi(r,\theta,t) &= \phi_0(r,t) + \sum_m \phi_m(r) e^{im\theta - i\omega t} \\ n(r,\theta,t) &= n_0(r,t) + \sum_m n_m(r) e^{im\theta - i\omega t}\end{aligned} \tag{6}$$

and averaging Eq. (5) averaged over θ. The first order and third order mean components of Eq. (5) give

$$\frac{\partial \langle n \rangle(r,t)}{\partial t} + \frac{1}{r}\frac{\partial}{\partial r}\langle r v_r n_i \rangle = 0 \tag{7}$$

$$\frac{\partial}{\partial t} r\langle n_i v_\theta \rangle + \frac{1}{r}\frac{\partial}{\partial r} r\left[\langle r n_i v_\theta v_r \rangle + m_i^{-1}\langle \pi_{r\theta}\rangle\right] = r\langle n_i g_\theta \rangle \tag{8}$$

where v_r and v_θ are the r,θ components of $\mathbf{v}_E = c\hat{z} \times \nabla\phi/B$ and $\langle r\pi_{r\theta}\rangle = (T_i/2\omega_{ci})\langle n_i(r\partial_r v_r - \partial_\theta v_\theta - v_r)\rangle$. In the limit $T_i = 0$ Eqs. (7) and (8) reduce to the quasilinear Eqs. (49) and (50) in Ref. 1. The fluctuating component of Eq. (5), neglecting mode-coupling terms is

$$-i(\omega - m\Omega)\delta n_{im} - \frac{icm}{Br}\frac{\partial n_0}{\partial r}\delta\phi_m + \nabla\cdot\left[\delta(n_i \mathbf{v}_i)^{(3)}_m\right] = 0 \tag{9}$$

where

$$\begin{aligned}\nabla\cdot\left[\delta(n_i\mathbf{v}_i)^{(3)}_m\right] = \frac{ic}{\omega_{ci}B}\Bigg\{ & n_0(\omega - m\Omega - \omega_{*i})\nabla^2\delta\phi_m + \tilde{\omega}\frac{dn_0}{dr}\frac{d\delta\phi_m}{dr} \\ & + \frac{2m\Omega}{r}\frac{dn_0}{dr}\delta\phi_m + m\frac{d\Omega}{dr}\frac{dn_0}{dr}\delta\phi_m + \frac{m}{r}\frac{d}{dr}\left[\frac{1}{r}\frac{d}{dr}(r^2\Omega)\right] n_0\delta\phi_m \\ & + \frac{mcT_i r}{e_i B}\frac{d}{dr}\left(\frac{1}{r}\frac{dn_0}{dr}\right)\frac{d}{dr}\left(\frac{\delta\phi_m}{r}\right) - \frac{mB}{cr}(r\Omega^2 + g)\delta n_{im} \\ & + \frac{mT_i}{re_i}\frac{d}{dr}\left(\frac{1}{r}\frac{d}{dr}(r^2\Omega)\right)\delta n_{im} + \frac{mT_i}{e_i} r\frac{d\Omega}{dr}\frac{d}{dr}\left(\frac{1}{r}\delta n_{im}\right)\Bigg\}\end{aligned} \tag{10}$$

and where the rotation and ion diamagnetic frequencies are defined by

$$\Omega = \frac{c}{Br}\frac{d\phi_0}{dr} \quad \text{and} \quad \omega_{*i} = \frac{mcT_i}{e_i Br}\frac{1}{n_0}\frac{dn_0}{dr}. \tag{11}$$

We define the Doppler-shifted frequency in the local rotating frame $\tilde{\omega} = \omega - m\Omega(r)$.

B. Electron Fluid Equations

Following Rosenbluth[3] we describe the electron fluid by $n = n_e^t + n_e^p$ where n_e^t is the density of electrons trapped in the central cell and n_e^p is the density of electrons passing through the central cell to the plugs or end cells.

Neglecting the collisional mixing between the two components we have

$$\frac{\partial n_e^{t,p}}{\partial t} + \nabla \cdot (n_e \mathbf{v}_e)^{t,p} = 0. \tag{12}$$

The trapped-electron component $E \times B$ drifts with the local potential of the central cell

$$(n\mathbf{v}_e)^t = \frac{cn_e^t}{B}\hat{z} \times \nabla\phi - \frac{cT_e}{eB}\hat{z} \times \nabla n_e^t \tag{13}$$

and the passing component $\mathbf{E} \times \mathbf{B}$ drifts with an average potential obtained from averaging ϕ over the central cell L_c, B_c, n_c and the plug plasma L_p, B_p, n_p. The precise definition and calculation of the electron-averaging operator requires the use of kinetic equations. Here we follow Rosenbluth[3] by taking the simple approximation that

$$\hat{\mathcal{L}}\phi = \langle \bar{\phi} \rangle = \left\langle \frac{1}{\tau} \int \frac{ds}{v_{||}} \phi_{cs} \right\rangle = L_c \phi_c / (L_c + L_p) \tag{14}$$

In Horton and Liu[1] a similar approximation is made by introducing the constant eigenvalue λ of the bounce-averaging operator $\hat{\mathcal{L}}$; however, no attempt is made in Ref. 1 to evaluate λ in terms of the central cell and plug plasma parameters.

In addition to the convective change in the trapped electron density given by

$$\delta n_e^p = -\frac{mc}{r\tilde{\omega}B} \frac{dn_{0e}^p}{dr} \delta\bar{\phi}, \tag{15}$$

there is an adiabatic change arising from the rapid transit motion given by

$$\delta n_{e||}^p = \frac{n_{0e}^p e(\delta\phi - \delta\bar{\phi})}{T_e} \tag{16}$$

as is well known from kinetic theory. The total passing electron density fluctuation is

$$\delta n_e^p = \frac{n_{0e}^p e(\delta\phi - \delta\bar{\phi})}{T_e} - \frac{mc}{rB\tilde{\omega}} \frac{dn_{0e}^p}{dr} \delta\bar{\phi} \tag{17}$$

and the trapped electron density fluctuation is

$$\delta n_e^t = -\frac{mc}{r\tilde{\omega}B} \frac{dn_{0e}^t}{dr} \delta\phi. \tag{18}$$

C. Radial Eigenvalue Equation

For low-frequency drift modes the electrostatic potential is governed by the condition of quasineutrality

$$n_i = n^t + n_e^p. \tag{19}$$

Evaluating the fluctuating part of Eq. (19) with Eqs. (9), (17), and (18) yields

$$-\frac{mc}{r\tilde{\omega}B}\frac{dn_{0i}}{dr}\delta\phi + \frac{\nabla\cdot\delta(n_i\mathbf{v}_i)_m^{(3)}}{i\tilde{\omega}} = -\frac{mc}{r\tilde{\omega}B}\frac{dn_{0e}^t}{dr}\delta\phi - \frac{mc}{r\tilde{\omega}B}\frac{dn_{0e}^p}{dr}\delta\bar{\phi} + \frac{en_{0e}^p}{T_e}(\delta\phi - \delta\bar{\phi}).$$

Using $n_{0i} = n_{0e}^t + n_{0e}^p$ and Eq. (10) for $\nabla\cdot(\delta n_i\mathbf{v}_i)_m^{(3)}$ yields the radial mode equation

$$\begin{aligned}\frac{c^2m_i}{e_iB^2}\Bigg\{&\nabla_\perp\cdot[n_0(\tilde{\omega}-\omega_{*i})\nabla_\perp\delta\phi] + m\frac{d\Omega}{dr}\frac{d}{dr}\left[n_0\left(1-\frac{\omega_{*i}}{\tilde{\omega}}\right)\delta\phi\right]\\ &+\Bigg[\left(2m\Omega + \frac{m^2(\Omega^2+g/r)}{\tilde{\omega}} - \frac{m^2cT_i}{\tilde{\omega}e_iBr^2}\frac{d}{dr}\left(r^2\frac{d\Omega}{dr}\right)\right)\left(\frac{dn_0}{rdr}\right) + \frac{m}{r}\frac{d}{dr}\left(\frac{1}{r}\frac{d}{dr}(r^2\Omega)\right)n_0\\ &+\frac{1}{r}\frac{d}{dr}(n_0\omega_{*i})\Bigg]\delta\phi\Bigg\} - \left(\frac{mc}{rB}\frac{dn_{0e}^p}{dr} + \frac{en_{0e}^p}{T_e}\tilde{\omega}\right)(\delta\phi - \langle\delta\bar{\phi}\rangle) = 0.\end{aligned} \tag{20}$$

Equation (20) includes the potential average term $\langle\delta\bar{\phi}\rangle$ which we need to model in order to make the two-dimensional integral-differential equation mathematically tractable. For modes that are essentially flute-like in the central cell with the fluctuating potential dropping to a small value in the plug the bounce average is approximately

$$\hat{\mathcal{L}}\delta\phi = \langle\delta\bar{\phi}\rangle = \lambda\delta\phi \cong \frac{L_c}{L_c+L_p}\delta\phi \tag{21}$$

which gives $1-\lambda = L_p/(L_c+L_p) \ll 1$. For strong mirror ratio at the end of the central cells $R = B_p/B_c$, assuming essentially mirror confinement for the bulk of the electrons, the density of passing electrons is small with

$$\frac{n_{0e}^p}{n_{0e}} \simeq \frac{1}{2(R+1)} \simeq \frac{B_c}{2B_p} \ll 1.$$

Taking these estimates into account the charge separation from the passing electrons in Eq. (20) may be written as

$$\frac{en_{0e}}{T_e}\left(\frac{n_{0e}^p}{n_{0e}}\right)\left(\frac{L_p}{L_c+L_p}\right)(\tilde{\omega}-\omega_{*e})\delta\phi_m$$

assuming that $\omega_{*e} = \omega_{*e}^p = -(mcT_e/reB)(d\ell n\ n_{0e}^p/dr)$.

Introducing a dimensionless parameter A_p measuring the ratio of the charge separation from passing electrons to that from the polarization current gives

$$A_p = \left(\frac{2n_{0e}^p}{n_0}\right)\left(\frac{a^2\omega_{ci}^2 m_i}{T_e}\right)\left(\frac{L_p}{L_c+L_p}\right) = 2\eta_p\left(\frac{a^2}{\rho_s^2}\right)\left(\frac{L_p}{L_c+L_p}\right) \simeq \frac{a^2 B_c L_p}{\rho_s^2 B_p L_c}. \tag{22}$$

By using Eqs. (21), and (22) we rewrite Eq. (20) as

$$\begin{aligned}
&\nabla_\perp\cdot[n_0(\tilde{\omega}-\omega_{*i})\nabla_\perp\delta\phi] + m\frac{d\Omega}{dr}\frac{d}{dr}\left[n_0\left(1-\frac{\omega_{*i}}{\tilde{\omega}}\right)\delta\phi\right] \\
&\quad + \left[\left(2m\Omega + \frac{m^2(\Omega^2+g/r)}{\tilde{\omega}}\right)\frac{1}{r}\frac{dn_0}{dr} - \frac{m\omega_{*i}}{r^2\tilde{\omega}}\frac{d}{dr}\left(r^2\frac{d\Omega}{dr}\right)\right. \\
&\quad \left. + \frac{m}{r}n_0\frac{d}{dr}\left[\frac{1}{r}\frac{d}{dr}(r^2\Omega)\right] + \frac{1}{r}\frac{d}{dr}(n_0\omega_{*i}) - \frac{2A_p n_0}{a^2}(\tilde{\omega}-\omega_{*e})\right]\delta\phi = 0.
\end{aligned} \tag{23}$$

Equation (23) with proper boundary conditions $\delta\phi_m(r\to 0) \simeq r^m$ and given $\delta\phi_m$ or $d\delta\phi_m/dr$ at $r = b$ determines the spectrum of eigenvalues for given radial profiles of $n_0(r)$ and $\phi_0(r)$.

In the limit in which the density gradients are weak compared with the potential gradients equation (24) reduces to

$$\nabla_\perp^2\delta\phi + \left\{\frac{md}{\tilde{\omega}rdr}\left[\frac{1}{r}\frac{d}{dr}(r^2\Omega)\right] - \frac{2A_p}{a^2}\right\}\delta\phi = 0. \tag{24}$$

$1/\tilde{\omega}$ term describes the interchange of vorticity $\varsigma = \dfrac{d(r^2\Omega)}{rdr} = \dfrac{d(rv_\theta)}{rdr}$. For the case $\dfrac{d\varsigma}{dr} \neq 0$ there is a restoring tendency of the perturbed flow discussed in Sec. IV.B.

To find the relation between Eq. (23) and the Rosenbluth-Simon equation[7] we use the linear Lagrangian displacement $\xi_m(r)$ from

$$\frac{d\xi}{dt} = \frac{cE_\theta}{B} \tag{25}$$

and rewrite the first-order ion-density fluctuation as

$$\delta n_m = -\xi_m\frac{dn_0}{dr}$$

where $\xi_m(r) = (mc/r\tilde{\omega}B)\delta\phi_m(r)$. The nonlinear Lagrangian displacement is analyzed in Sec. IV.C.

Rewriting Eq. (23) in terms of $\xi_m(r)$ yields

$$\frac{1}{r}\frac{d}{dr}\left(r^3 n_0\tilde{\omega}(\tilde{\omega}-\omega_{*i})\frac{d\xi_m}{dr}\right)+\left[(1-m^2)n_0\tilde{\omega}(\tilde{\omega}-\omega_{*i})\right.$$
$$\left.+\left(\omega^2+\frac{m^2 g}{r}\right)r\frac{dn_0}{dr}-\frac{2A_p n_0 r^2\tilde{\omega}(\tilde{\omega}-\omega_{*e})}{a^2}\right]\xi_m=0. \qquad (26)$$

The boundary conditions on ξ are $\xi(r\to 0)\simeq r^{m-1}$ and given $\xi(b)$ or $d\xi(b)/dr$. For the $A_p=0$ case Eq. (26) reduces to the well known Rosenbluth-Simon[7] equation for flute modes in a cylindrical plasma.

Equation (26) is the generalization of Eq. (28) in Ref. 1 for the electron drift mode in a rotating plasma when the axial eigenvalue λ from the electron bounce averaging operator in Eq. (24) of Ref. 1 is related to A_p through $1-\lambda=2\alpha^2 A_p$. With this relation, Eq. (24) of Ref. 1 is the same as Eq. (23) in this work. For large A_p values, $A_p\simeq 1/2\alpha^2$, the passing electron contribution dominates and gives the electron drift wave with $\tilde{\omega}\simeq \omega_{*e}A_p/(A_p+\nu_{m,n})$. The electron dissipation $i\delta_e(k)$ retained in Ref. 1, but neglected in the present work, drives the electron drift wave unstable.

III. Analytic Solutions for Solid Body Rotation

Here we summarize the dispersion relation[8] for solid body rotation Ω =constant, with the Gaussian density profile and linear gravity

$$n_0(r)=n_0\exp(-r^2/a^2)\ ,\ g(r)=g_0 r/a.$$

The eigenvalue Eq. (23) reduces to

$$\frac{d^2\delta\phi}{dr^2}+\left(\frac{1}{r}-\frac{2r}{a^2}\right)\frac{d\delta\phi}{dr}+\left(\frac{2}{a^2}\nu-\frac{m^2}{r^2}\right)\delta\phi=0 \qquad (27)$$

where we define the eigenvalue ν by

$$\nu(\omega,m,\Omega,A_p,g_0/a,T_i/T_e)=-\frac{1}{\tilde{\omega}(\tilde{\omega}-\omega_{*i})}\left[m^2\left(\Omega^2+\frac{g_0}{a}\right)+\tilde{\omega}(2m\Omega+\omega_{*i})\right.$$
$$\left.+A_p\tilde{\omega}(\tilde{\omega}-\omega_{*e})\right]. \qquad (28)$$

The solution of Eq. (27) is given by either $\delta\phi_{m,n}(r) = A_m \frac{a}{r} \exp(r^2/a^2) W_{p,q}(r^2/a^2)$ where $W_{p,q}(x)$ is the Whittaker function[8] with $p = (\nu_{m,n}+1)/2$ and $q = m/2$; or equivalently the confluent hypergeometric function

$$\delta\phi_{m,n}(r) = A_{m,n} \left(\frac{r}{a}\right)^m {}_1F_1\left(\frac{m}{2}+1-\nu_{m,n}, m+1; \frac{r^2}{a^2}\right).$$

The eigenvalues determined by boundary conditions $\delta\phi_{m,n}(b) = 0$ are

$$\nu_{m,n}(b/a) = m + 2n + f(b/a) \tag{29}$$

and are shown in Fig. 1. The index $n = 0, 1, 2, \ldots$ is the radial mode number of $\delta\phi_m(r)$, and $f_{m,n}(b/a)$ is a monotonically decreasing function with the limit $b/a \to \infty$, $f(b/a) \to 0$.

The dispersion relation following from Eq. (28) is

$$A\tilde{\omega}^2 + B\tilde{\omega} + C = 0 \tag{30}$$

where

$$\begin{aligned} A &= \nu_{m,n} + A_p \\ B &= 2m\Omega + \omega_{*i}(1-\nu_{m,n}) - A_p\omega_{*e} \\ C &= m^2\left(\Omega^2 + \frac{g_0}{a}\right). \end{aligned} \tag{31}$$

The quadratic Eq. (30) gives instability for $C > 0$ driven by the centrifugal force of rotation. The stabilization arises from $B \neq 0$ due to the charge separation from the Coriolis force, the finite Larmor radius effect[2,6,7] and the axial motion of the passing electrons.[3-5] The passing electron contribution has the opposite sign to the finite Larmor radius effect whereas the Coriolis force effect can reinforce either the passing electron ($\Omega < 0$) or the finite Larmor radius effect ($\Omega > 0$).

The effective gravity g_0 may be due to either the ponderomotive force from radio frequency fields or the curvature of the magnetic field lines. For the case where g is dominated by the curvature of the axisymmetric magnetic field lines we remove the scaling of g by introducing $g_0 = (c_s^2 a/L^2)\hat{g}$ with the dimensionless $\hat{g}$ given by

$$\hat{g} = \frac{3a^4}{2\rho_s^2} \frac{\int_1^2 \left(\frac{1}{B^2}\frac{dB}{dz}\right)^2 dz}{\int_1^2 \frac{dz}{B^2}} \tag{32}$$

which is order unity in terms of the gyroradius and aspect ratio scaling. The maximum value of $\hat{g}$ is given by the infinite parabolic mirror field $B = B_0(1 + z^2/L^2)$ and where $\hat{g} = 3a^4/4L^2\rho_s^2$.

In this analytic model the frequency and growth rate are functions of the six dimensionless parameters

$$m, \hat{\Omega},\ \hat{g},\ A_p,\ \frac{b}{a},\ \frac{T_i}{T_e},$$

and units of frequency are $c_s\rho_s/a^2$.

The dimensionless frequency and the dimensionless growth rate given by the quadratic dispersion relation (30) in the laboratory frame are

$$\begin{aligned} \omega &= m\hat{\Omega} + \frac{m}{\nu_{m,n} + A_p}\left[A_p - \hat{\Omega} - \frac{T_i}{T_e}(\nu_{m,n} - 1)\right] \\ g &= \frac{m}{\nu_m + A_p}\left[(\nu_{m,n} + A_p)\left(\hat{\Omega}^2 + \hat{g}\right) - \left(\hat{\Omega} + \frac{T_i}{T_e}(\nu_{m,n} - 1) - A_p\right)^2\right]^{1/2} \end{aligned} \tag{33}$$

respectively.

The discriminant determining stability (in the dissipationless limit) is given by

$$D = B^2 - 4AC = 4m^2\left\{\left[\hat{\Omega} + \frac{T_i}{T_e}(\nu_{m,n} - 1) - A_p\right]^2 - \left(\hat{g} + \hat{\Omega}^2\right)(\nu_{m,n} + A_p)\right\}. \tag{34}$$

The stabilizing condition is given by $D > 0$. From (34) we can give the stabilizing condition as

$$\begin{aligned} &A_p^2 - \left[\hat{\Omega}(\hat{\Omega} + 2) + \hat{g} + 2\frac{T_i}{T_e}(\nu_{m,n} - 1)\right]A_p \\ &- \left[(\nu_{m,n} - 1)\left(\hat{\Omega} - \frac{T_i}{T_e}\left(\nu_{m,n}^{1/2} + 1\right)\right)\left(\hat{\Omega} + \frac{T_i}{T_e}\left(\nu_{m,n}^{1/2} - 1\right)\right) + \nu_{m,n}\hat{g}\right] \geq 0. \end{aligned} \tag{35}$$

For given m, $\hat{\Omega}$, $\hat{g}$, we can determine critical A_p for stability. We find that a good approximation for the critical density, above which the drift mode is stable in the absence of electron dissipation, is

$$(A_p)_{\text{crit}} \equiv A_p^s \simeq \hat{\Omega}(\hat{\Omega} + 2) + \hat{g} + 2\frac{T_i}{T_e}(\nu_{m,n}(b/a) - 1). \tag{36}$$

The stability boundaries determined by (35) are shown in Figs. 2-7. We discuss the different effects on stability as follows.

A. Effect of Passing Electrons

For low rotational speeds there is in general both a critical or threshold value A_p^c and a cut-off value A_p^s for the passing electron density. For unstable modes $A_p^c < A_p < A_p^s$. For A_p below threshold A_p^c the stable region in $\hat{\Omega}$ is determined by finite Larmor radius effects through $(T_i/T_e)(\nu_{m,n} - 1)$ and the value of $\hat{g}$.

For reference parameters we take $\hat{g} = 0$ which implies just enough quadrupole or rf stabilization to balance the bad axisymmetric curvature, $T_i/T_e = 1$, and $b/a = 3$. The stable region determined by competition between the passing electrons and the FLR effect for m=1 and 2 are shown in Fig. 2(a). For m=1, when $A_p \gtrsim 0.1$, the window, $-2 < \hat{\Omega} < 0$, is stable. As shown in the detail, Fig. 2(b), when A_p is very small, say $A_p < 10^{-2}$, the stability of the system is determined by the FLR effect. For $A_p = 0$, the stable window is $0 \lesssim \Omega < 2$. As A_p is increased, this window becomes narrower, vanishing altogether for $A_p > 1.5 \times 10^{-2}$. The stability boundaries for m=2 are similar to those for m=1 except in scale. The $A_p < A_p^c$ stable window for the m=2 case does not vanish until $A_p \simeq 1$ due to the stronger influence of the FLR effect. When $A_p > A_p^s$, given by Eq. (36), the stable region determined by passing electrons appears.

For $\hat{g} = +1$, a typical value for an axisymmetric system with no rf stabilization, there are unstable regions for all $\hat{\Omega}$ for $0 < A_p < 2$ for the m=1 mode and for $0 < A_p < 4$ for the m=2 as shown in Fig. 3.

For $\hat{g} = -1$ corresponding to a strongly quadrupole or rf stabilized system the m=1 mode has a stable window for $-2.7 < \hat{\Omega} < +1.2$ for all A_p as shown in Fig. 4. The m=2 mode is stable for $-1 \lesssim \hat{\Omega} \lesssim 1$ for all A_p.

B. Effect of the Ratio of the Wall-to-Plasma Radius

Now we consider the effect of varying the wall-to-plasma radius ratio b/a. Decreasing b/a may be viewed as the relaxation of the original plasma profile from the instabilities or from other transport processes. In the analytic model used here there is an edge or wall plasma density given by $n(b)/n(0) = \exp(-b^2/a^2)$. For the values of $b/a = 3, 2, 1$ the edge-to-central density ratios are 10^{-4}, .02 and .37, respectively.

We use $\hat{g} = 0$ and $\hat{\Omega} = -4$ as the reference values for varying the plasma-to-wall radius. In Fig. 5 we show the effect of decreasing b/a. As the wall is brought into the plasma, the m=1 growth rate increases as $(\nu_{1,0}(b/a) - 1)^{1/2}$ whereas the finite Larmor radius stabilization increases as $(T_i/T_e)\,(\nu_{1,0}(b/a) - 1)$. For small b/a first the m=3 and finally the m=2 mode become stabilizied; however, the m=1 mode remains unstable until $b \simeq a$. The effect of the wall-to-plasma radius on the threshold density is shown by comparing Fig. 6-7 for $b/a = 1$ with Fig. 3-4 for $b/a = 3$. For $\hat{g} = +1$ the A_p required for stabilization of the m=1 mode increases from $A_p(b/a = 3) = 2$ to $A_p(b/a = 1) = 10$ shown in Fig. 6. The same tendency is shown in Fig. 7 for the $\hat{g} = -1$ case.

Thus we find that as b/a decreases from 3 to 1 the finite Larmor radius effects opens up a stable window for $-2 < \hat{\Omega} < 2.5$ and $A_p < A_p^c \sim 4$ but for $\hat{\Omega} < -2$, typical of tandem mirror rotations, there is a substantial increase in the A_p required for stability, $A_p > A_p^s(b/a)$, with decreasing b/a. The results with $A_p = 0$ agree well with those of Pearlstein and Freidberg.[9]

The result of varying b/a has an important implication for the quasilinear evolution of the system. As the quasilinear relaxation in Eqs. (7) and (8) takes place, the plasma radius becomes a function of time $a(t)$ and increases toward b. The stability analysis implies that in the final stages of evolution only the m=1 mode is unstable and that there may be a marginally stable quasilinear steady state for $a(t \to \infty) \simeq b$. In this final state the plasma is poorly confined with $n(b)/n(0) \simeq 1/3$ for the Gaussian density model.

C. Effect of Varying the Quadrupole or RF Fields

The effect of varying the quadrupole or rf fields is parameterized by the value of $\hat{g}$. Changing the system from a strongly unfavorable effective gravity $\hat{g} = +1$ to a strongly favorable effective gravity $\hat{g} = -1$ is shown by comparing Figs. 3 and 4. For $\hat{g} = +1$ the system is unstable to m=1 and m=2 modes for all $\hat{\Omega}$ unless the passing electron density parameter A_p exceeds the cut-off value $A_p > A_p^s$. For strongly favorable $\hat{g}$ there is a stable rotational window for $|\hat{\Omega}| \leq 1$ for m=1 and m=2 for all values of A_p.

For faster rotational speeds $\hat{\Omega} > |\hat{g}|$ the value of $\hat{g}$ is of secondary importance compared with the values of A_p and b/a in determining the stability of the system.

IV. Differential Rotation and Passing Particles

For general profiles of density and potential that evolve from background transport processes the stability analysis must be performed numerically. In this section we use the well-known shooting method to find the eigenvalues and wavefunctions from Eq. (23). In this study we restrict consideration to the simple boundary condition $\delta\phi_m(r = b) = 0$.

The profiles used in the study are Gaussian and parabolic for the density

$$n_g(r) = n_0 \exp(-r^2/a^2) \tag{37}$$

$$n_p(r) = n_0(1 - r^2/b^2) \tag{38}$$

and the inverse tangent for the rotational speed

$$\Omega(r) = c_1 \tan^{-1}\left(\frac{r - r_1}{\Delta r}\right) + c_2 \tag{39}$$

where c_1 and c_2 are given in terms of the central rotation frequency $\Omega_0 = \Omega(r = 0)$ and the edge rotation frequency $\Omega_b = \Omega(r = b)$ by

$$c_1 = \frac{\Omega_b - \Omega_0}{\tan^{-1}\left(\frac{b - r_1}{\Delta r}\right) + \tan^{-1}\left(\frac{r_1}{\Delta r}\right)}$$

$$c_2 = \Omega_0 + c_1 \tan^{-1}\left(\frac{r_1}{\Delta r}\right).$$

and Δr is the parameter controlling the steepness of the gradient in $\Omega(r)$. The potential $\phi_0(r)$ and rotational $\Omega(r)$ profiles used in the study are shown in Fig. 8.

The accuracy of the eigenvalue solver is tested by taking the limit $\Omega_b = \Omega_0$ which gives $c_1 = 0$ and $\Omega(r) = \Omega_0$=constant and comparing the results with the analytic solutions given in Eq. (34) for a Gaussian density profile.

A. Differential Diamagnetic Drifts

For the parabolic density profile (39) the diamagnetic drifts $\omega_{*e}(r)$ are strongly increasing functions of radius. In this subsection we keep the $\mathbf{E}\times\mathbf{B}$ rotation rigid at $\Omega = \Omega_0$ and show that the change from a Gaussian to a parabolic density profile is strongly stabilizing for comparable mean density gradients. (As usual in changing a profile, an exact comparison is not possible since it depends on choosing some arbitrary constraints.) The decreased growth rate is expected from the local approximation since the dispersion of the wave frequency $\omega_*(r)$ with radius weakens coherence of the modes. For the parabolic density we note that although $\omega_*(r) \to \infty$ as $r \to b$ the function $n(r)\omega_*(r)$ in Eq. (23) remains finite for $0 \le r \le b$.

The unstable modes in the spectrum $m = 1-10$ are shown in Fig. 9. The width of the unstable spectrum is limited by FLR effects that are enhanced by the radial dispersion from $\omega_*(r)$. A similar result is given by Bowers and Haines[10] when they take a cut-off Gaussian density profile and Ω=const in their numerical solutions.

In the presence of $\omega_*(r)$ the modes develop radially outgoing and incoming wave components given by $k_r = (2i)^{-1}(\delta\phi_m^*\partial_r\delta\phi_m - \phi_m\partial_r\delta\phi_m^*)$ which, in contrast, is zero (standing wave) for the ω_*=constant Gaussian profile. The wavefunction for the parabolic profile is peaked closer to the plasma in radial position than the Gaussian wavefunction consistent with the local approximation. The change in the wavefunction is shown in Figs. 10(a,b) which compares the $m = 1, 2, 3$ modes for the parabolic and Gaussian profiles and gives their respective frequencies and growth rates. The preferred stability of the parabolic profile suggests that quasilinear relaxation may drive the system toward states with variations in $\omega_*(r)$ subject to the constraints imposed by particle sources and sinks.

B. Differential E × B Rotation

For the Gaussian density profile with constant ω_{*e} we decrease the speed of rotation of the outer plasma by varying Ω_b from Ω_0 to zero. A smaller Ω_b than Ω_0 is observed in the experiments[11] and may result from collisional ion viscosity in the edge plasma or charge exchange collisions with the higher edge neutral density component.

In Fig. 11a we show the m=1 growth rate as a function of decreasing edge plasma speed Ω_b. With the central plasma rotating at $\Omega_0 = 2\omega_{*i}(\hat{\Omega} = -4$ for $T_i = T_e)$ the solid body growth rate is $\gamma_1 \cong 2\left[\rho_s c_s/a^2\right]$ for $A_p \leq 2$ as given by Eq. (33) and shown in Fig. 11a at $\Omega_b = \Omega_0$. As the edge speed drops to zero the growth rate decreases even for $A_p = 0$. Part of the decrease in the growth rate is accounted for by the decrease in the average equivalent solid body rotational speed defined by a comparison of the profiles at constant rotational energy or constant angular momentum. The remaining stabilization arises from the differential rotation.

Figure 11b shows the same parameter variation for the m=2 mode which has the solid body growth rate $\gamma_2 \cong 4\left[\rho_s c_s/a^2\right]$ for $\Omega_b = \Omega_0$. Again the growth rate decreases strongly as Ω_b goes to zero.

Changing to a parabolic density profile combines the stabilizing effects of $\omega_*(r)$ and $\Omega(r)$ and is shown in Fig. 12a for m=1 and Fig. 12b for m=2.

The stabilizing effect of the differential rotation on the interchange instability driven by the centrifugal force acting on the density gradient is understood from the change in the topology of the eigenfunctions. As the interchange of the plasma from $\delta n = -\xi \partial n_0/\partial r$ takes place to release the energy density $\delta W = \frac{1}{2} m_i \delta n r \Omega^2 \xi = -\frac{1}{2} m_i r(\partial n_0/\partial r)\Omega^2 \xi^2$ the tongues of displaced plasma are wrapped back in azimuthal angle (entrained) which decreases the amount of interchanged plasma. Mathematically, the falling behind or entrainment of the tongues is given by the phase shift that the eigenfunction develops from the dispersion in $\tilde{\omega} = \omega - m\Omega(r)$. Comparison of Figs. 10(a) and (b) shows an example of the phase shift.

We take the wavefunction $\delta\phi_m(r)$ as real in the interior of the plasma and write $|\delta\phi_m| \cos\left[m\theta - \omega t + \beta(r)\right]$ for the phase shift arising from the complex wavefunc-

tion $\delta\phi_m(r) = |\delta\phi_m| \exp[i\beta(r)]$ for $r > 0$. We may estimate the value of β by integrating Eq. (26) across the resonant layer defined by $\mathrm{Re}(\omega) = m\Omega(r_m)$ while neglecting $\beta(r)$ in all terms except the second derivative term. These approximations lead to

$$\frac{d\delta\phi_m}{dr} = \frac{d}{dr}|\delta\phi_m| + i|\delta\phi_m|\frac{d\beta}{dr} \simeq \frac{F_0|\delta\phi_m|}{\omega - m\Omega(r)}$$

for r sufficiently near the resonance $\Omega(r_m) = \mathrm{Re}\omega/m$. Integrating through the resonance gives $\beta(r) = \pi F_m/m|d\Omega/dr|$ where F_m is a constant. This simple calculation of $\beta(r)$ is useful for understanding the origin of β, but the value of $\beta(r)$ is computed from the $\arg[\delta\phi_m(r)]$.

The change in the topology of the wavefunctions is shown in Figs. 13 and 14, which give the contours of constant $\phi(r,\theta,t) = \phi_0(r) + |\delta\phi_m(r)|\cos[m\theta + \beta(r) - \omega t]$ for a typical (25%) amplitude of the wave. The spiraling of the tongues of plasma develops in the vicinity of the resonant layers. In contrast for solid body rotation the wavefunction is purely real ($\beta \equiv 0$) and the tongues or arms are pure radial displacements with symmetry about the radial axes of the arms at $\theta_n = 2\pi n/m$ with $n = 1, 2, \ldots m$.

A dynamical picture of the stability effect of the differential rotation follows from the vorticity theory of instability given by Lin.[12] In this argument the flow $V_\theta = r\Omega$ is decomposed into the sum of flows from vortex filaments. The interchange of a strong and weak vortex filament is shown to result in a perturbed flow that restores the original configuration provided the gradient of the vorticity does not vanish. In our problem, the effective vorticity is $\varsigma = d(rV_\theta)/rdr$ and the non-vanishing gradient condition is equivalent to $F = d\varsigma/dr \neq 0$ which follows from the stability analysis of Eq. (24).

The free energy stored in the sheared flow is destabilizing only for reversed flows where $\Omega(b)\Omega(0) < 0$ as shown in Figs. 11 and 12. The states with $\Omega(b) \simeq 0$ are approximately the most stable states between the limits of the solid body rotational instability and the Kelvin-Helmholtz instability.

C. $\mathbf{E} \times \mathbf{B}$ Transport

From the particle point of view the favorable effect of the sheared rotation on stability is related to the confining of the $\mathbf{E} \times \mathbf{B}$ excursions of the interchanged particles by the sheared rotation.

As shown in Ref. 1 the linear plasma displacement $\xi = \mathrm{cm}\delta\phi_m/rB\tilde{\omega}$ obtained from $d\xi/dt = cE_\theta/B$ fails for $|r - r_m| \leq \Delta r_t$ where $\Delta r_t = (c\phi_m/rB|d\Omega/dr|)^{1/2}$. The plasma in this region becomes trapped in a vortical flow due to the $\mathbf{E} \times \mathbf{B}$ convection in the resonant layer. The situation is similar to the rapid transport across a sheared magnetic field due to a resonant magnetic perturbation.

Knowing the linear eigenfunctions it is straightforward to study the transport across the sheared layer by integrating the equations of motion $d\boldsymbol{\xi}/dt = \mathbf{v}_E$ for the test fluid cells. Here we analyze the fluid trajectories close to the resonance. Finding all orbits for a given $\phi(r, \theta, t)$ is equivalent to solving the continuity equation, Eq. (1) to first order in ε, for the density $n(r, \theta, t)$ given the initial distribution $n(r, \theta, 0)$.

Introducing $I = r^2/2$ as action variable the equations of motion $\dot{r} = v_{Er}$, $r\dot{\theta} = v_{E\theta}$ are a 1-1/2 D Hamiltonian system with

$$\frac{dI}{dt} = -\frac{c}{B}\frac{\partial\phi}{\partial\theta} = \frac{c}{B}\sum_m m|\phi_m(r)|\sin\left[m\theta - \omega t + \beta(r)\right] \tag{40}$$

$$\frac{d\theta}{dt} = \frac{c}{B}\frac{\partial\phi}{\partial I} = \Omega(r) + \frac{c}{rB}\frac{\partial}{\partial r}\sum_m |\phi_m(r)|\cos\left[m\theta - \omega t + \beta\right] \tag{41}$$

where $r = (2I)^{1/2}$. For a single mode the motion is integrable and reduces to the pendulum equation for $|\delta v_{E\theta}| \ll r\Omega$. In this approximation we transform to the waveframe with $\psi = \theta - \omega t/m$ and obtain

$$\frac{d\psi}{dt} = \Omega - \frac{\omega}{m} = \left.\frac{d\Omega}{dr}\right|_{r_m} \Delta r(t) \tag{42}$$

$$\frac{d\delta r}{dt} = \frac{\mathrm{cm}|\varphi_m|}{r_m B}\sin(m\psi + \beta_m) \tag{43}$$

where $\beta_m = \beta(r_m)$. For $d\Omega/dr < 0$ the motion (42) and (43) has stable fixed points at $\psi = (2\pi p\beta_m)/m$ with $p = 0, 1, 2, \ldots, m-1$. The reduced Hamiltonian is

$$H_m^{\mathrm{res}}(\Delta r, \psi) = \frac{1}{2}\left(\frac{d\Omega}{dr}\right)_m \Delta r^2 - \frac{c|\varphi_m|}{rB}\cos(m\psi + \beta_m) \tag{44}$$

where the effective mass of the fluid particle increases with shear. The equation for the separatrix between trapped and circulating motion is

$$\Delta r_{sx}(\psi) = \pm 2 \left(\frac{c|\varphi_m|}{r_m B |d\Omega/dr|} \right)^{1/2} \sin\left(\frac{m\psi + \beta_m}{2} \right), \tag{45}$$

and the characteristic frequency $\omega_b^{n\ell}$ for convection around the vortex is

$$\omega_b^{n\ell} = m r_t \left| \frac{d\Omega}{dr} \right| = m \left(\frac{c|\varphi_m|}{r_m B} \left| \frac{d\Omega}{dr} \right| \right)^{1/2}. \tag{46}$$

Global stochasticity occurs either from the presence of a second wave[13,14] with $\omega_b^{n\ell} \approx |\omega_1 - \omega_2|$ or the resonance $\omega_0^{n\ell} \simeq n\pi v_{\|}/L$ due to the overlapping of the nonlinear resonances. The situation is mathematically similar to the enhanced transport due to the overlapping of magnetic islands produced by magnetic perturbations in a sheared magnetic field.

Even in the presence of a single mode the radial excursions $\Delta r = \pm \Delta r(\psi)$ with frequency $\omega_b^{n\ell}$ of the $\mathbf{E} \times \mathbf{B}$ drifting guiding centers will produce an enhanced collisional transport from the broken symmetry of the equilibrium. The drift mode enhanced transport can exceed the quadrupole induced transport for a critical value of the wave amplitude. Formulas (44)-(46) show that differential $\mathbf{E} \times \mathbf{B}$ rotation not only tends to stabilize the modes, but reduces the anomalous transport produced by the modes.

In the limit of solid body rotation the Hamiltonian becomes simply

$$H^{sb} = \Omega I + \frac{c}{B} \sum_{m,n} \varphi_{mn}(r) \cos(m\theta - \omega t + \beta_m^0) \tag{47}$$

with $\varphi_{mn}(r)$ real and Ω and β_m^0 constants. The $\mathbf{E} \times \mathbf{B}$ transport for this type of system is studied by Kleva and Drake[13] and Horton.[14] They show that the motion, which at small φ_{mn} is bounded by the nodes of $\varphi_{mn}(r)$, becomes globally stochastic when a generalized resonance overlap criterion is satisfied. For the low m modes the width of the radial convection increases from that given in Eq. (45) with $\Delta r \sim a(\tilde{\phi}/\Delta\phi_0)^{1/2}$ for sheared rotation to $\Delta r \sim a$ for solid body rotation.

V. Summary and Conclusions

In this work we analyze the drift mode stability of the rotating plasma including the effect of differential $\mathbf{E} \times \mathbf{B}$ rotation, sheared diamagnetic drifts and the role of passing electrons in stabilizing the rotational instabilities of a tandem mirror system.

The basic stability equation for the system is derived from the ion and electron hydrodynamic equations with a two component electron fluid description given by Rosenbluth[3] describing the trapped and passing electron dynamics. The mode equation contains the finite Larmor ion radius, the Coriolis force and the passing electrons as sources of charge separation that influence the stability of the centrifugal force driven interchange mode. The equation is shown to be related to that given by Horton and Liu[1] with a reinterpretation of the axial eigenvalue problem and that given by Kesner and Lane[5] from a fluid limit of the electrostatic Vlasov-quasineutral system of equations.

The stability analysis shows that solid body rotation with a Gaussian density profile, which allows analytic solution, is substantially more unstable than the profiles with differential rotation with $E \times B$ and diamagnetic drifts. For sufficiently strong shear the radial gradient of the angular momentum will drive a Kelvin-Helmholtz type of instability;[14] however, sheared flows stronger than those expected for the tandem mirror are required for the onset of these modes as shown in Figs. 11 and 12 for particular examples. Below the onset of the sheared flow instabilities the change in the topology of the interchange wave function, as shown in Fig. 13 and Fig. 14, produced by the differential flows greatly reduces the effectiveness of the density gradient or pressure gradient driven interchange instability.

The critical passing electron density required for stability $A_p^s(\Omega, b/a, T_i/T_e)$ is given approximately by Eq. (36) which agrees well with the exact results given in Figs. 2-4, and 6-7.

The stability analysis shows that there are a number of combinations of differential flows and passing electron density values that produce stable system when electron dissipation is neglected.

For the low m modes considered here it is shown that the growth rate begins to increase from the free energy in the sheared rotation only after the flow becomes reversed

at radial boundary. Similarly the introduction of differential rotation in the diamagnetic drift frequencies by a broader density profile distorts the wave function and substantially reduces the growth rates. For example the change to a parabolic density profile gives the growth rate spectrum shown in Fig. 9 which has γ_m monotonically decreasing with m and only m=1 and m=2 modes unstable for $T_i = T_e$.

We observe that stabilization by large $A_p > A_p^s(\Omega, b/a, T_i/T_e)$ tends to push the wave frequency in the laboratory toward zero which is detrimental for plasma confinement since the m=2 asymmetries of the laboratory plasma then resonate with the wave.

Differential $\mathbf{E} \times \mathbf{B}$ rotation with small A_p may be the preferred method of stabilizing the interchange modes. An analysis of the $\mathbf{E} \times \mathbf{B}$ transport of test fluid particles or guiding center motion of the particles is given which shows the importance of differential $\mathbf{E} \times \mathbf{B}$ rotation for the control of anomalous transport. For comparable wave amplitudes the cross-field transport in the presence of differential rotation is confined to resonant layer of width $\Delta r \simeq a(\tilde{\phi}_m/\Delta\phi_0)^{1/2}$ compared with that from solid body rotation which extends over the whole width of the plasma once the amplitudes exceed a small critical value depending on the wave frequency $\tilde{\omega}$ in the plasma rest frame.

In conclusion, we suggest that a plasma starting with constant Ω and ω_* profiles will tend to be strongly unstable and would evolve through quasilinear relaxation and mode coupling, as constrained by background transport and injection processes, towards more stable configurations with substantial differential rotation in the profiles. We note that only small changes in the potential profile are required to produce substantial changes in the stability of the plasma.

Acknowledgements

This paper was supported by the U.S. Department of Energy Contract no. DE-FG05-80ET-53088.

References

1. W. Horton and J. Liu, Phys. Fluids **27**, 2067 (1984).
2. J.D. Freidberg and D.A. D'ipollito, Phys. Fluids **26**, 2657 (1983).
3. M.N. Rosenbluth, Physica Scripta T2, 104 (1982).
4. H. Berk, M.N. Rosenbluth, V. Wong, T.M. Antonsen, and D. Baldwin, Sov. Phys. Plasma **9**, 176 (1983).
5. J. Kesner and B. Lane, Phys. Fluids **28**, 634 (1985).
6. J. Liu, "The Linear instability and nonlinear motion of rotating plasma," Ph.D. Thesis (University Microfilms, Ann Arbor, 1985).
7. M.N. Rosenbluth and A. Simon, Phys. Fluids **8**, 1300 (1965).
8. A.B. Mikhailovskii, "Theory of Plasma Instabilities", vol. 2 (Consultants Bureau, New York-London, 1974) pp. 123-124.
9. J.P. Freidberg and L.D. Pearlstein, Phys. Fluids **21**, 1207 (1978).
10. E. Bowers and M.G. Haines, Phys. Fluids **14**, 165 (1971).
11. E.B. Hooper, Jr., G.A. Hallock, and H.H. Foote, Phys. Fluids **26**, 314 (1983).
12. C.C. Lin, "The theory of hydrodynamic stability" (Cambridge Univ. Press, 1966) pp. 56-58.
13. R.G. Kleva and J.F. Drake, Phys. Fluids **27**, 1686 (1984).
14. W. Horton, Plasma Physics and Controlled Fusion **27**, 937 (1985) and Plasma Physics **23**, 1107 (1981).
15. F.W. Perkins and D.L. Jassby, Phys. Fluids **14**, 102 (1971).

Figure Captions

1. The lowest eigenvalues $\nu_{m,n}(b/a)$ of the Whittaker equation for solid body rotation and a gaussian density profile.

2a. The stability boundaries in the plane representing passing particle density, A_p, and solid body rotation frequency, Ω, with $\hat{g} = 0$, $T_i/T_e = 1$, $b/a = 3$, and $m = 1, 2$.

2b . Small A_p detail of the m=1 stability boundaries showing the stable window for $A_p < A_p^c$ which was not visible in Fig. 2(a).

3. The same as Fig. 2 with an unfavorable radial well, $\hat{g} = +1$.

4. The same as Fig. 2 with a favorable radial well, $\hat{g} = -1$.

5. The variation of the low-m growth rates with wall-to-plasma radius ratio, b/a, for solid body rotation, $\Omega = -4$, and Gaussian density profile.

6. The same as Fig. 3 with $\hat{g} = +1$, but $b/a = 1$.

7. The same as Fig. 4 with $\hat{g} = -1$, but $b/a = 1$.

8. Typical profiles of the equilibrium potential and the sheared rotational frequency, $\Omega(x)$, used in the study of differential $\mathbf{E} \times \mathbf{B}$ rotation. Here, the on-axis rotation rate is $\Omega_0 = -4$, the edge rotation is $\Omega_b = 0$, $\Delta r/a = 0.1$ and $r_1/a = b/2a$.

9. Low-m spectra for solid body rotation, $\Omega = -4$, Gaussian density profile with $T_i/T_e = 1, 2$ and parabolic profile with $T_i/T_e = 1$.

10a. The wave functions vs. $x = r/a$ for $m = 1, 2, 3$, with solid body rotation, $\Omega = -4$, $T_i/T_e = 1$, and a Gaussian density profile. The imaginary parts of the wave functions vanish.

10b. The real and imaginary parts of the wave functions vs. $x = r/b$ for $m = 1, 2, 3$, with solid body rotation, $\Omega = -4$, $T_i/T_e = 1$, and a parabolic density profile.

11a. The real and imaginary frequencies versus the edge plasma rotation frequency, Ω_b, for the m=1 mode and varying A_p. The density profile is a Gaussian with $b/a = 2$, $\Delta r/a = 0.1$, $r_1/a = 1$, and $T_i/T_e = 1$. The central rotation rate is $\Omega_0 = -4$, so that $\Omega_b = -4$ corresponds to solid body rotation.

11b. The same as Fig. 11(a) for the m=2 mode.

12a. The same as Fig. 11(a) for a parabolic density profile, m=1 mode. The shear parameters here are scaled to the plasma radius, $\Delta r/b = 0.1$ and $r_1/b = 0.5$.

12b. The same as Fig. 12(a) for the m=2 mode.

13. The contours of constant potential in the laboratory frame which are the instantaneous flow lines of the (clock-wise) $\mathbf{E} \times \mathbf{B}$ guiding-center motion. Shown is the m=2 mode of the solid body rotating plasma for a Gaussian density profile. The amplitude of the perturbation is taken as $\max(\delta\phi)_m = 0.25\phi_0(r = 0)$.

14. The same as Fig. 13 for a differentially rotating plasma. The rotational profile is as shown in Fig. 8.

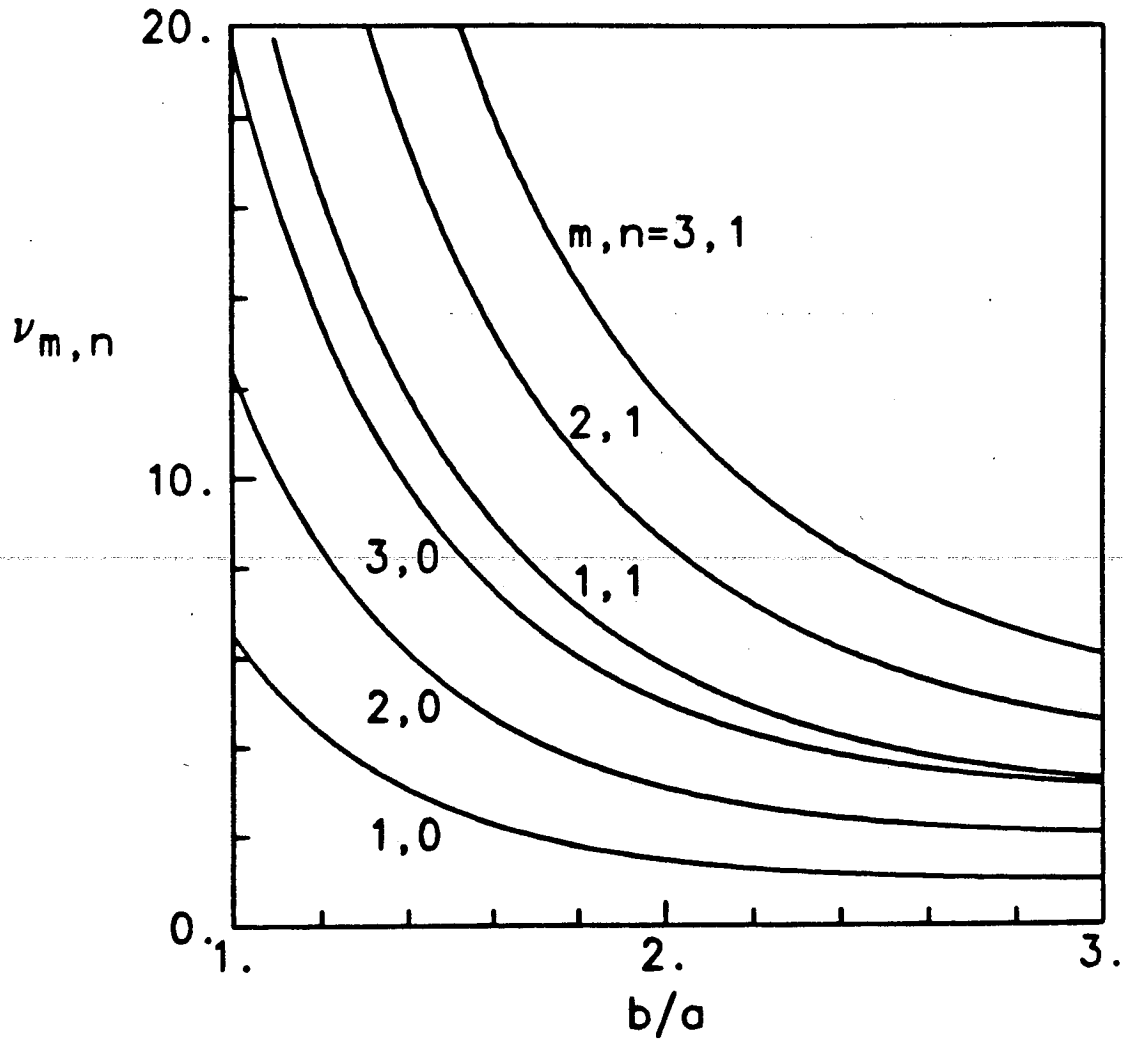

Fig. 1

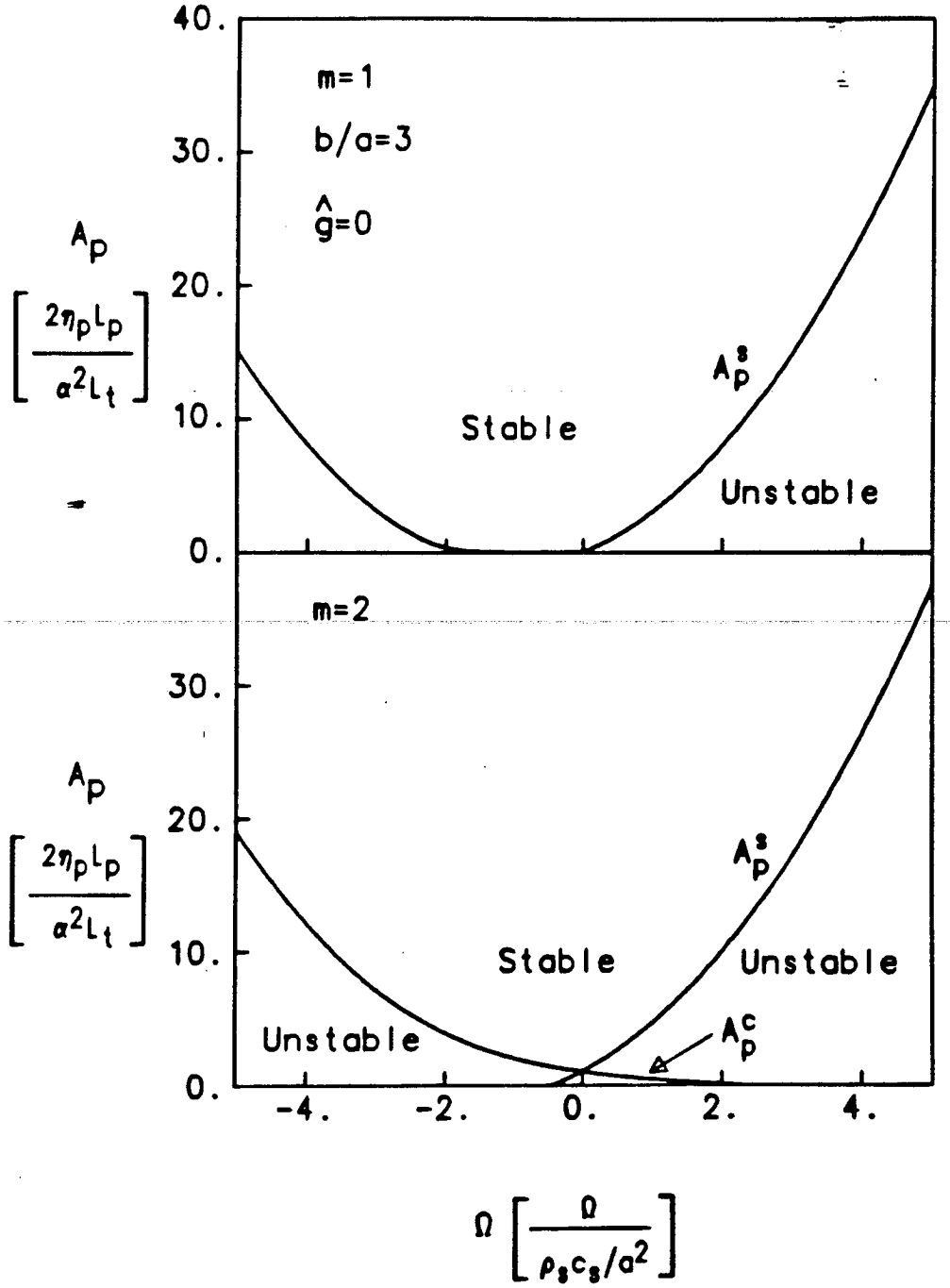
40.
30.
20.
10.
0.
m=1
b/a=3
ĝ=0
A_p
$\left[\frac{2\eta_p L_p}{a^2 L_t}\right]$
A_p^s
Stable
Unstable
m=2
A_p^c
Unstable
-4.
-2.
0.
2.
4.
$\Omega\left[\frac{\Omega}{\rho_s c_s/a^2}\right]$

Fig. 2

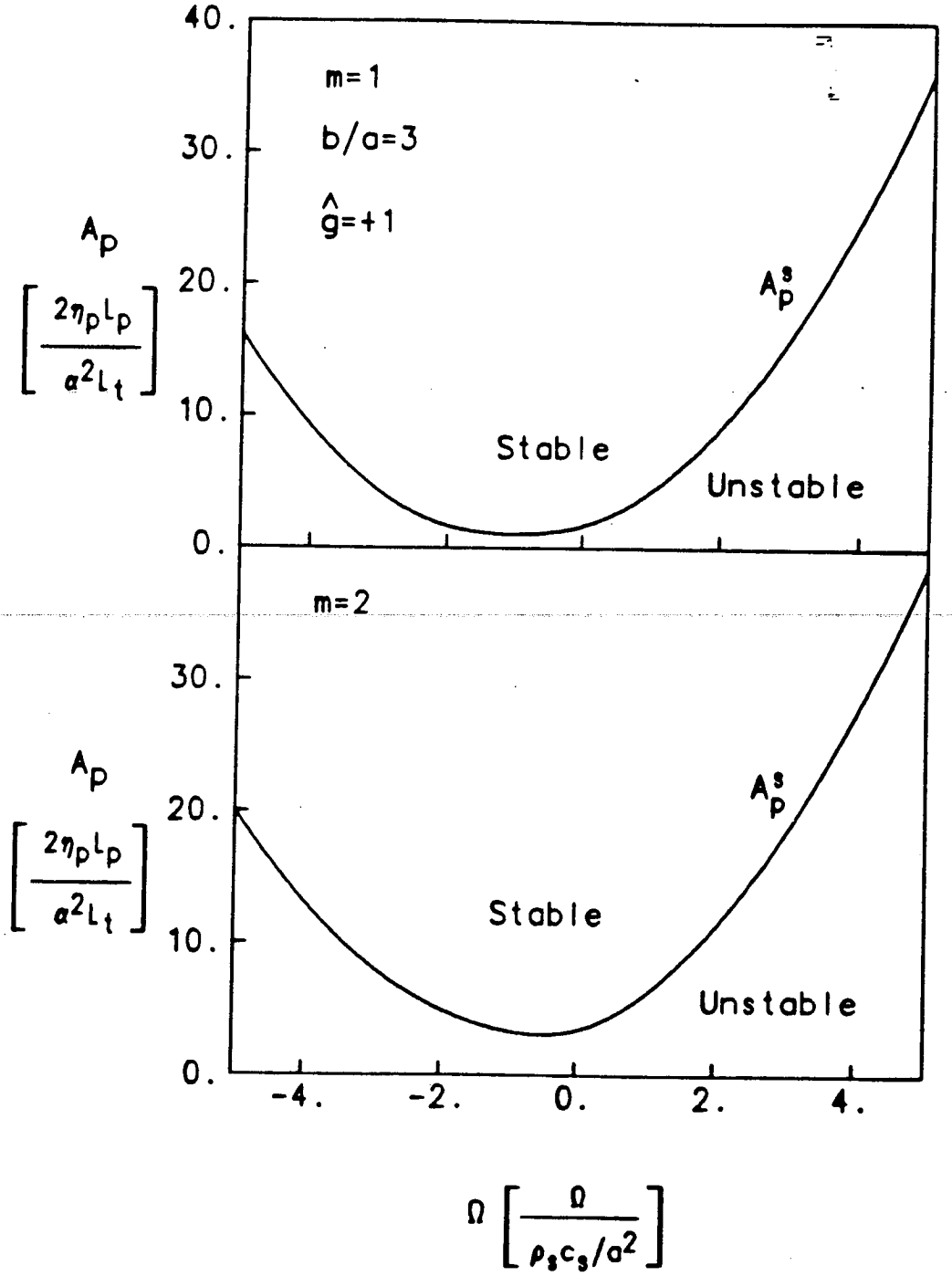
40.
30.
20.
10.
0.
m=1
b/a=3
ĝ=+1
A_p
$\left[\frac{2\eta_p l_p}{a^2 l_t}\right]$
A_p^s
Stable
Unstable
m=2
30.
20.
10.
0.
A_p
$\left[\frac{2\eta_p l_p}{a^2 l_t}\right]$
A_p^s
Stable
Unstable
-4.
-2.
0.
2.
4.
$\Omega\left[\frac{\Omega}{\rho_s c_s/a^2}\right]$

Fig. 3

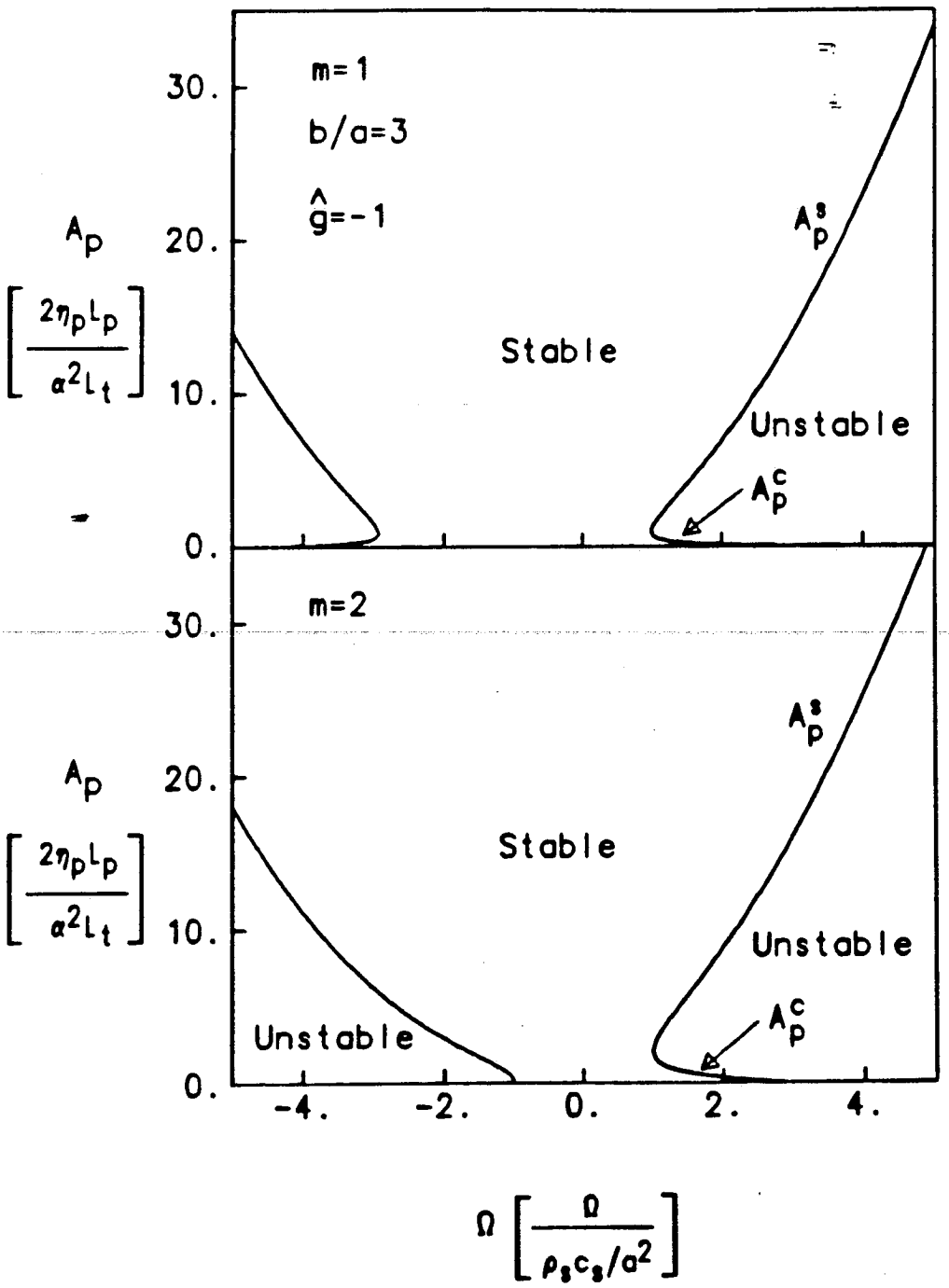
m=1
b/a=3
$\hat{g}$=-1
A_p
$\left[\frac{2\eta_p L_p}{\alpha^2 L_t}\right]$
30.
20.
10.
0.
Stable
Unstable
A_p^s
A_p^c
m=2
Stable
Unstable
Unstable
-4.
-2.
0.
2.
4.
$\Omega\left[\frac{\Omega}{\rho_s c_s/a^2}\right]$

Fig. 4

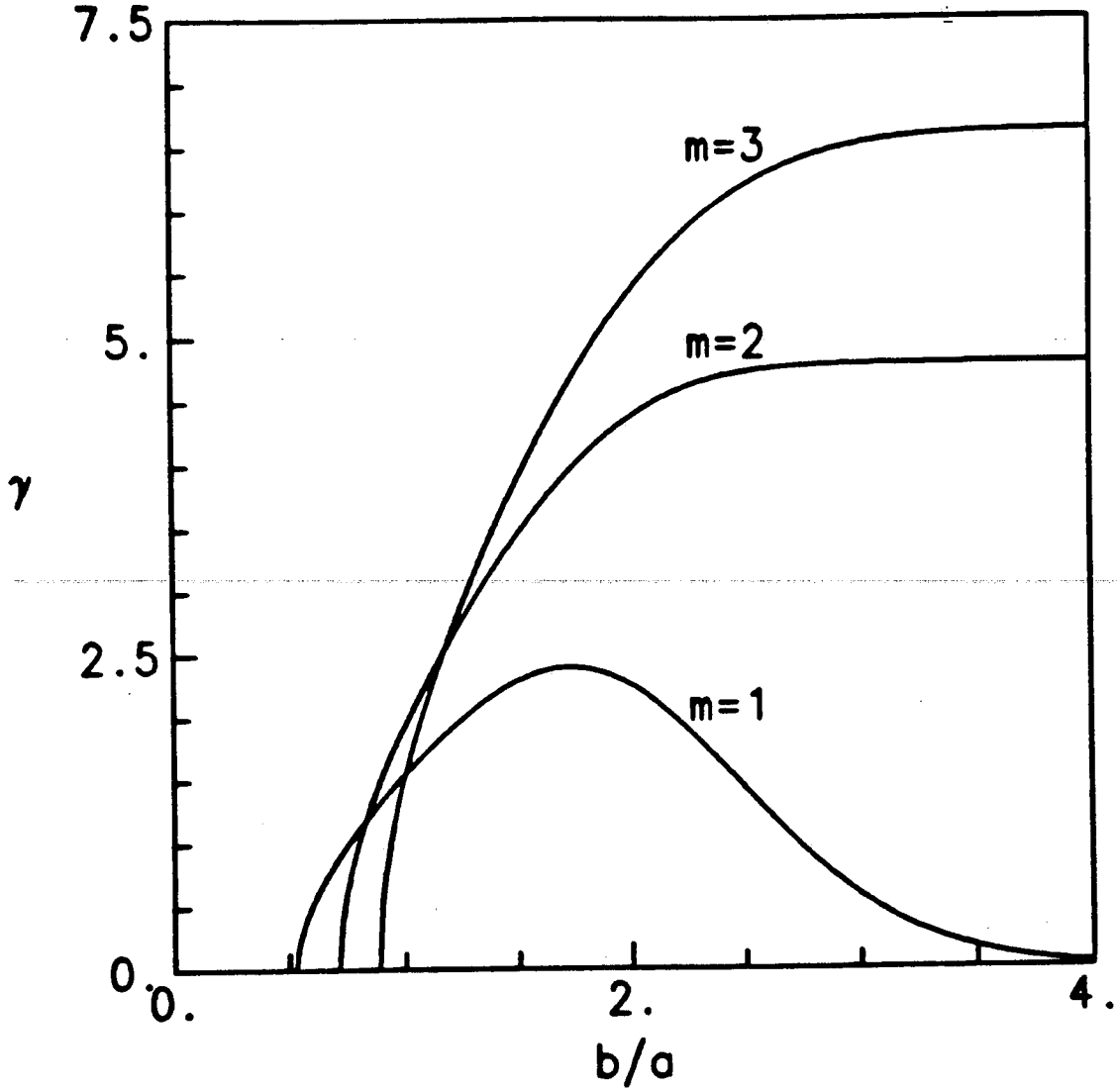

Fig. 5

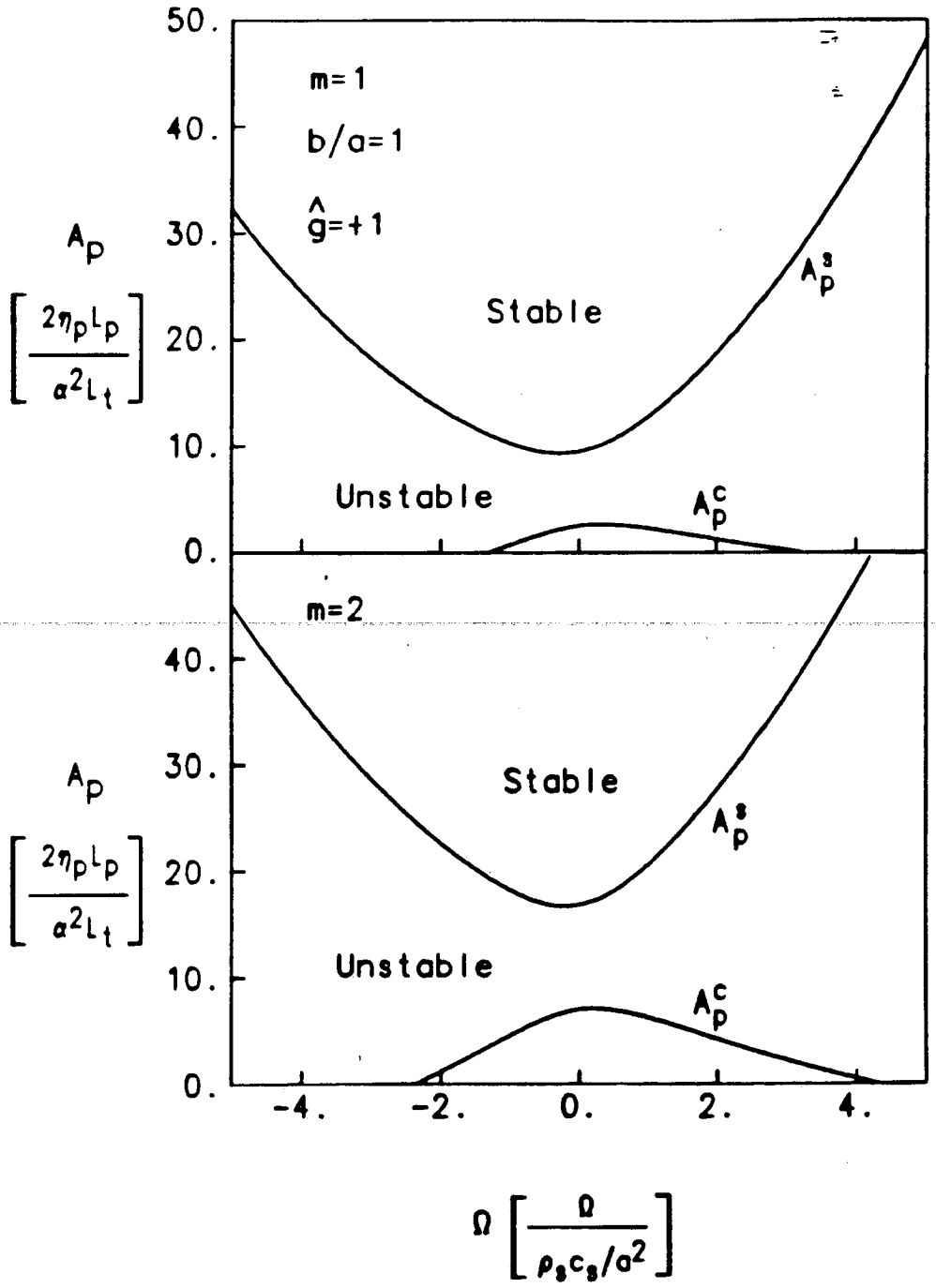
50.
40.
30.
20.
10.
0.
m=1
b/a=1
ĝ=+1
Stable
Unstable
A_p^s
A_p^c
$A_p \left[\frac{2\eta_p l_p}{a^2 l_t}\right]$
m=2
-4.
-2.
0.
2.
4.
$\Omega \left[\frac{\Omega}{\rho_s c_s / a^2}\right]$

Fig. 6

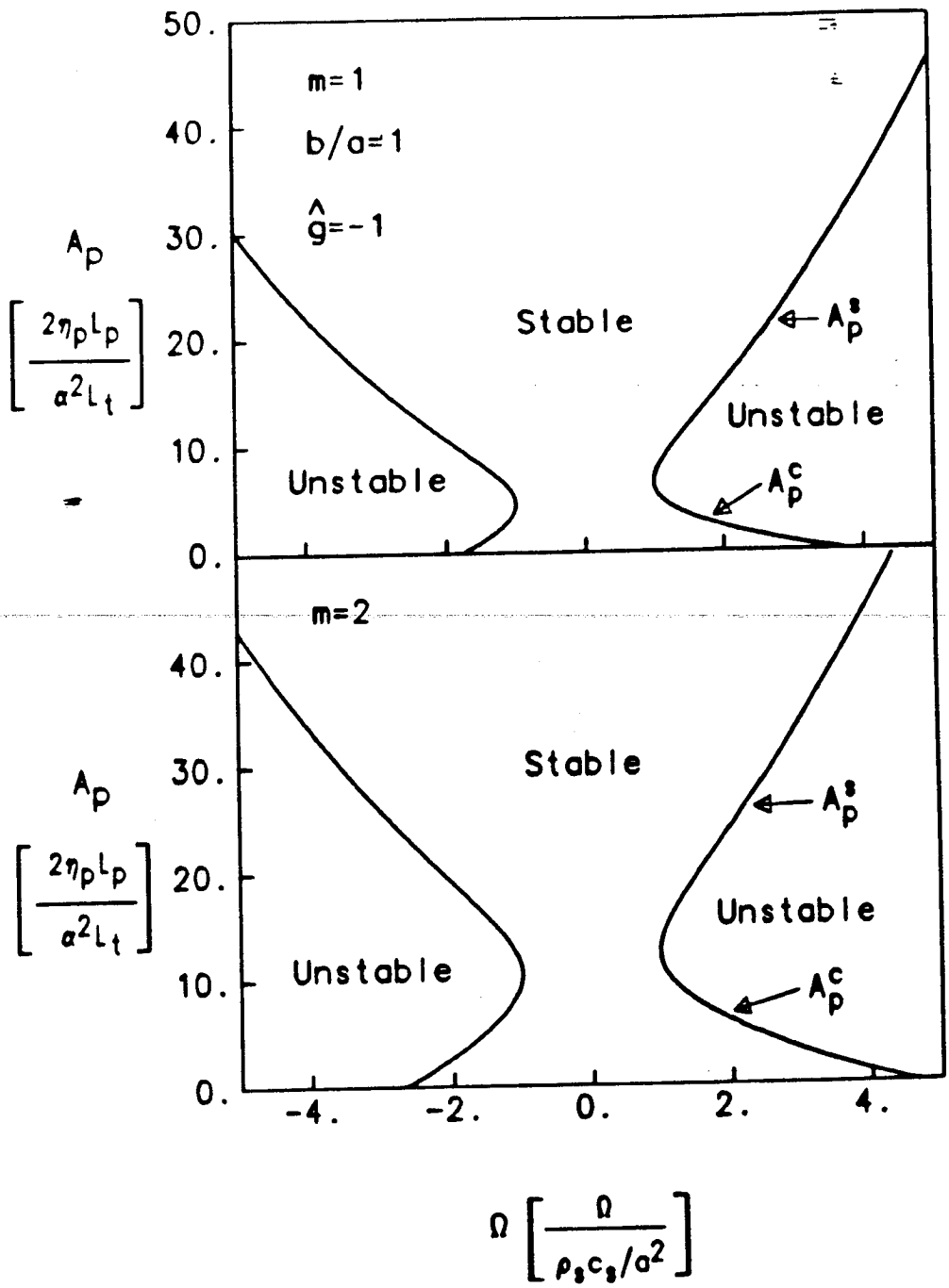
m=1
b/a=1
ĝ=-1
Stable
Unstable
Unstable
A_p^s
A_p^c
m=2
Stable
Unstable
Unstable
A_p^s
A_p^c
$A_p \left[\frac{2\eta_p L_p}{a^2 L_t}\right]$
50.
40.
30.
20.
10.
0.
-4.
-2.
0.
2.
4.
$\Omega \left[\frac{\Omega}{\rho_s c_s / a^2}\right]$

Fig. 7

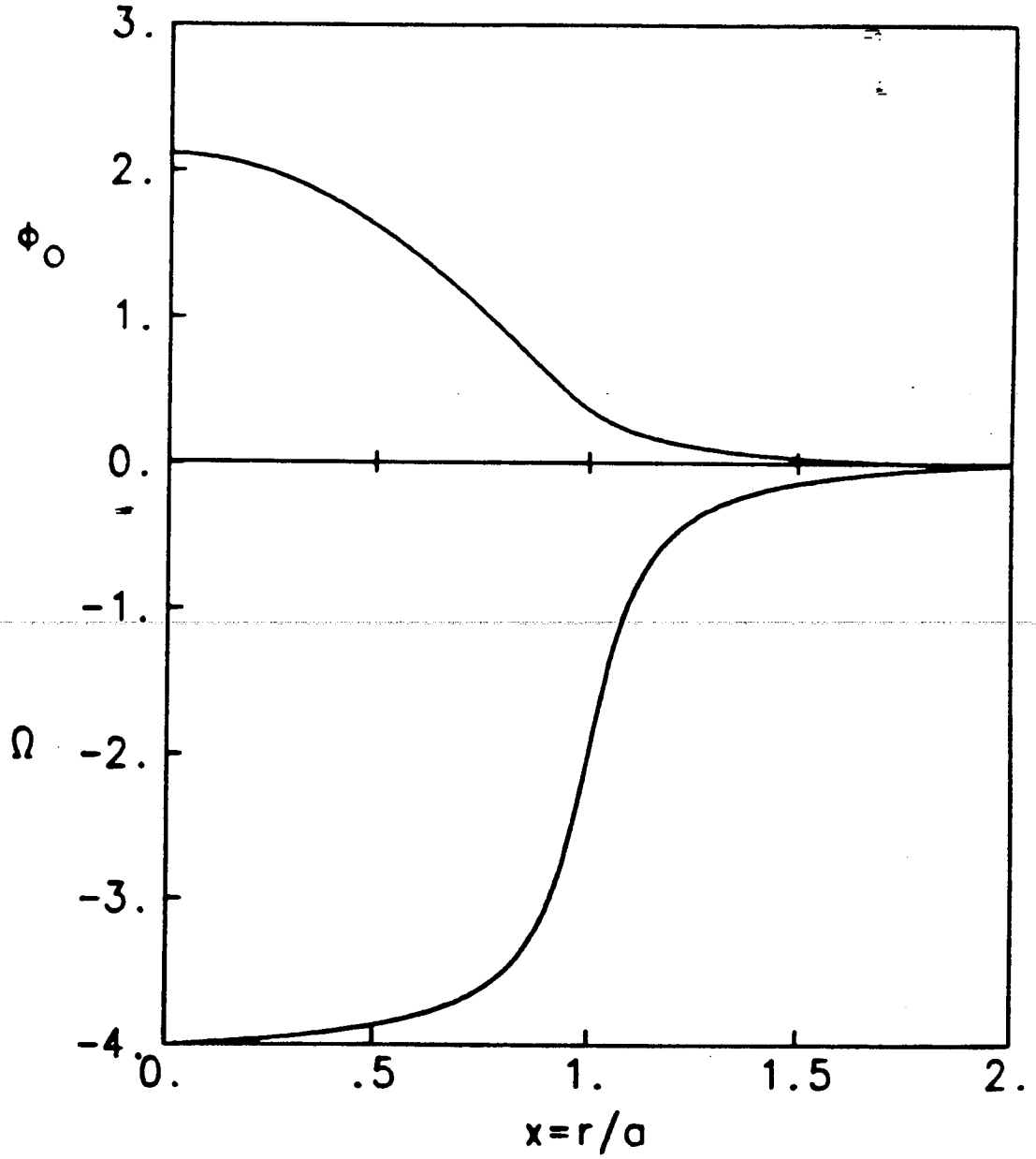

Fig. 8

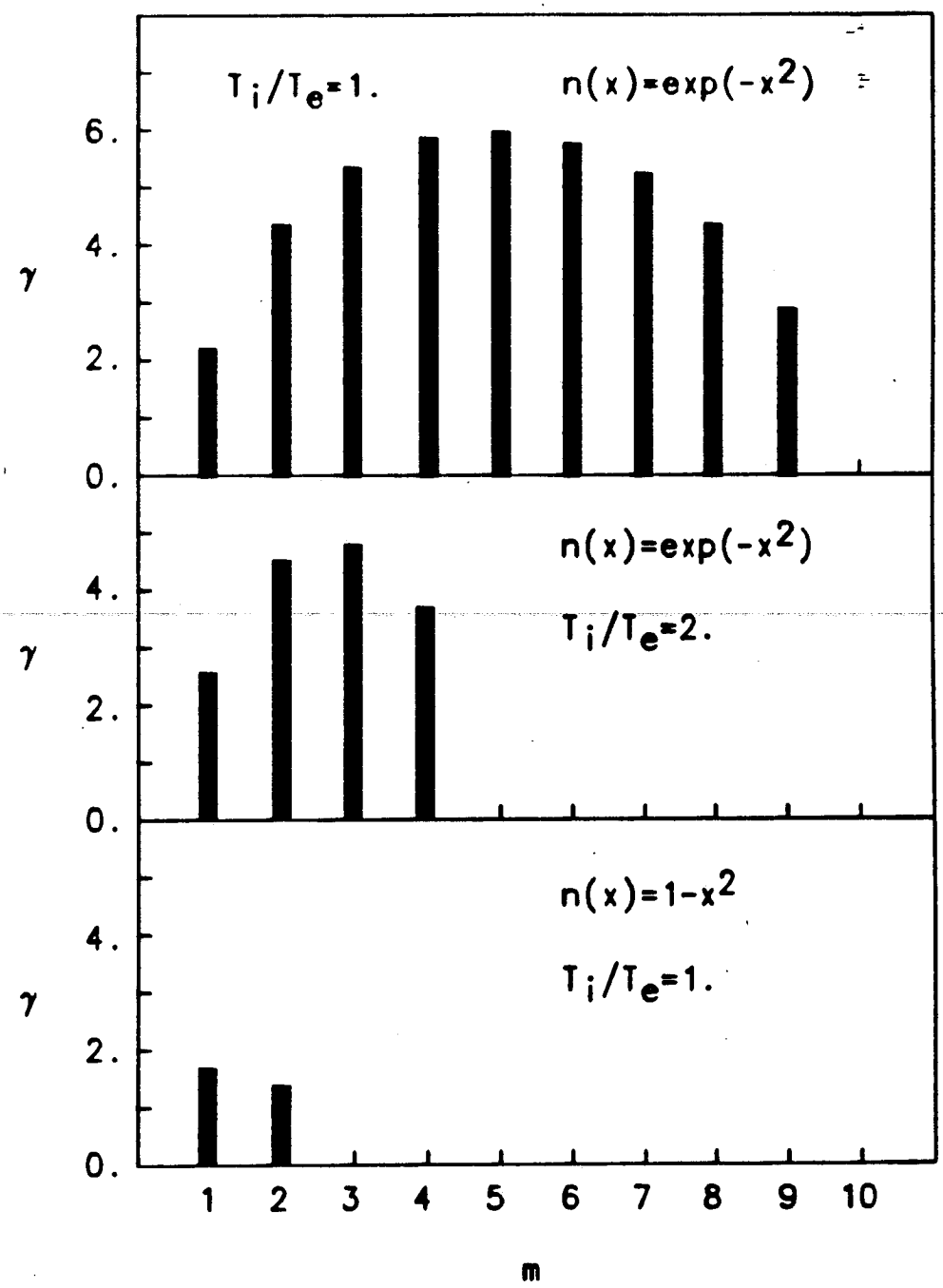
T_i/T_e=1.
n(x)=exp(-x^2)
n(x)=exp(-x^2)
T_i/T_e=2.
n(x)=1-x^2
T_i/T_e=1.
γ
6.
4.
2.
0.
1
2
3
4
5
6
7
8
9
10
m

Fig. 9

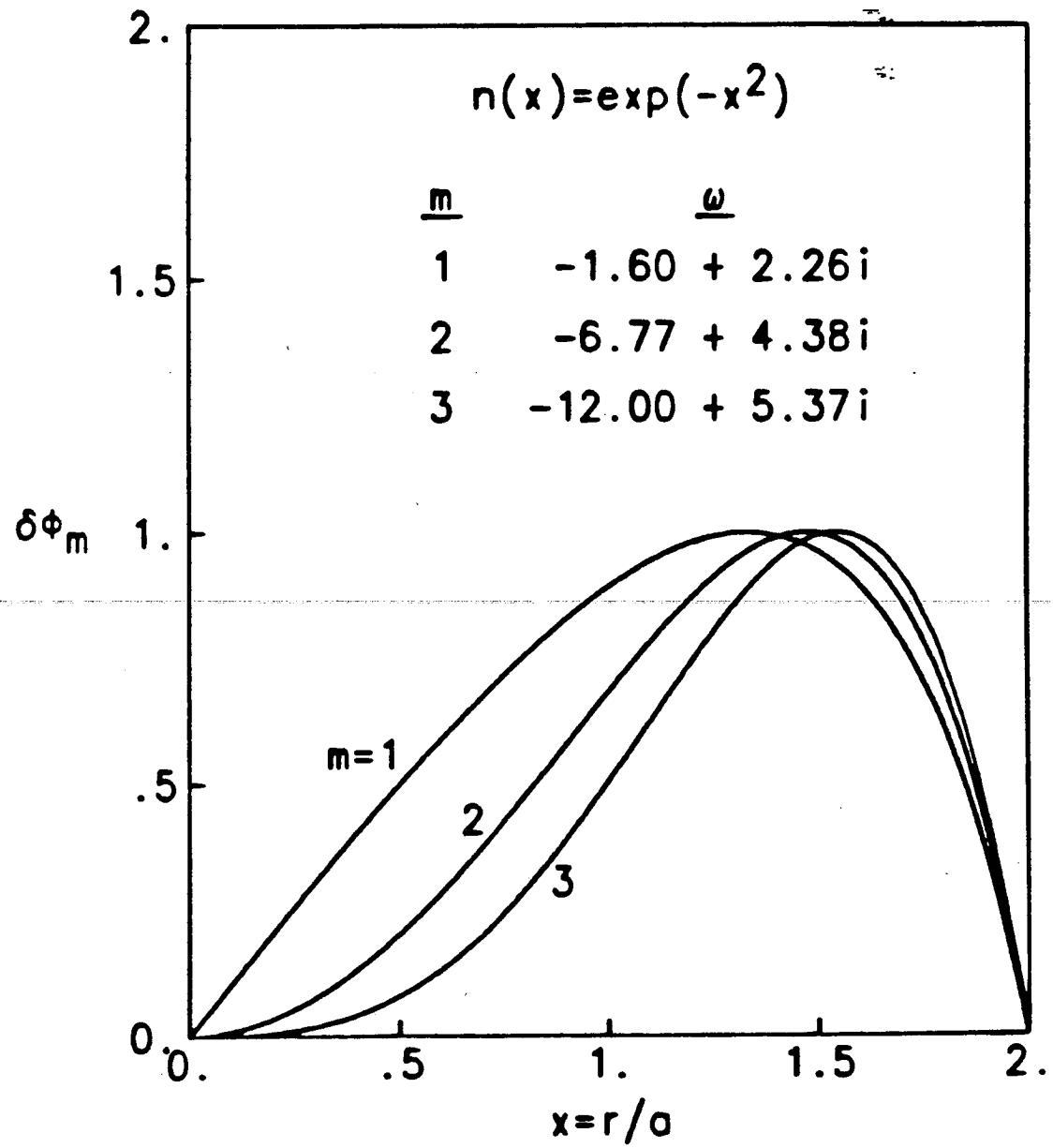
n(x)=exp(-x²)
m
ω
1
-1.60 + 2.26i
2
-6.77 + 4.38i
3
-12.00 + 5.37i
δΦm
2.
1.5
1.
.5
0
0.
.5
1.
1.5
2.
x=r/a
m=1
2
3

Fig. 10(a)

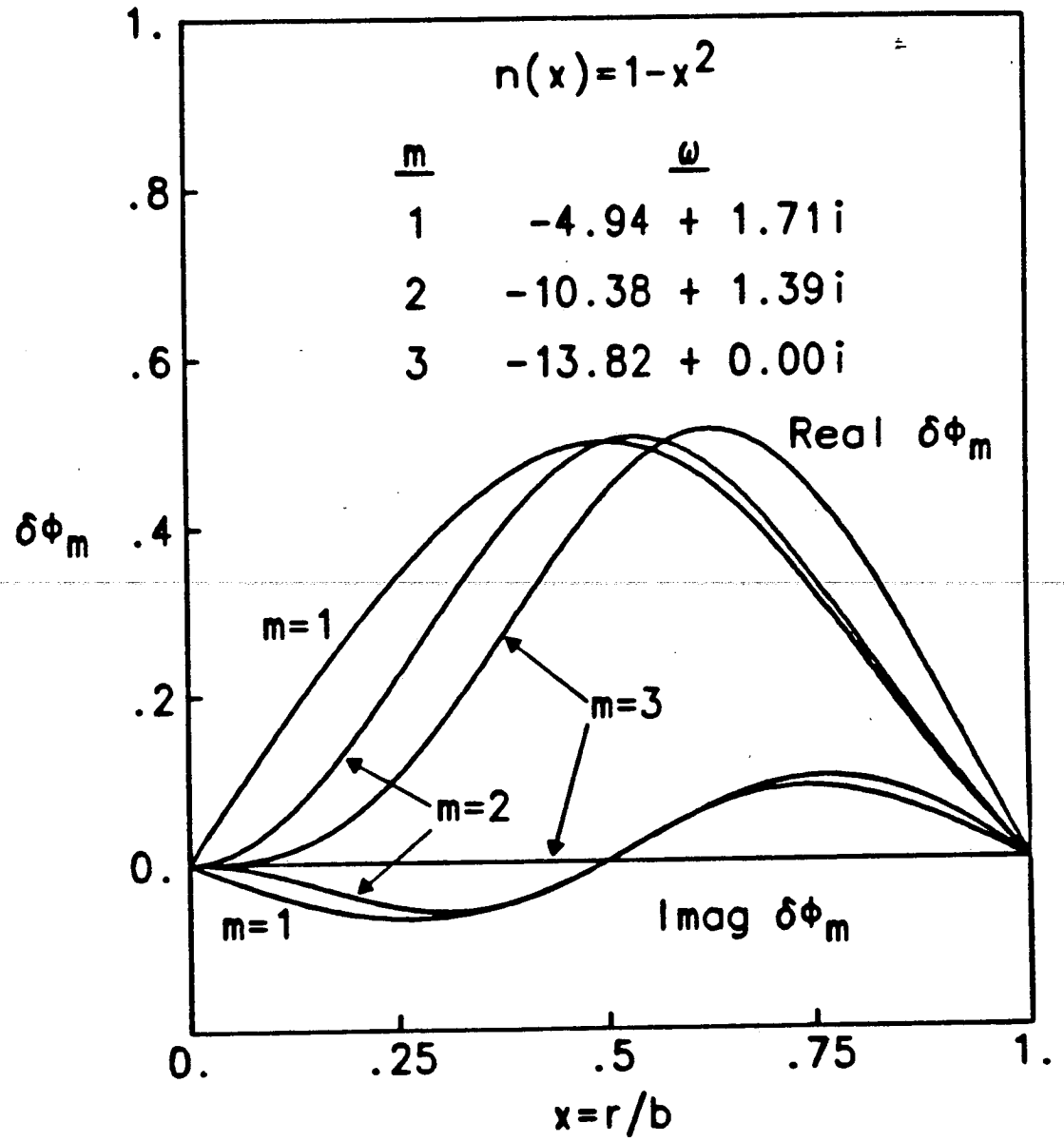
n(x)=1-x²
m
ω
1
-4.94 + 1.71i
2
-10.38 + 1.39i
3
-13.82 + 0.00i
Real δΦm
Imag δΦm
δΦm
m=1
m=2
m=3
m=1
1.
.8
.6
.4
.2
0.
0.
.25
.5
.75
1.
x=r/b

Fig. 10(b)

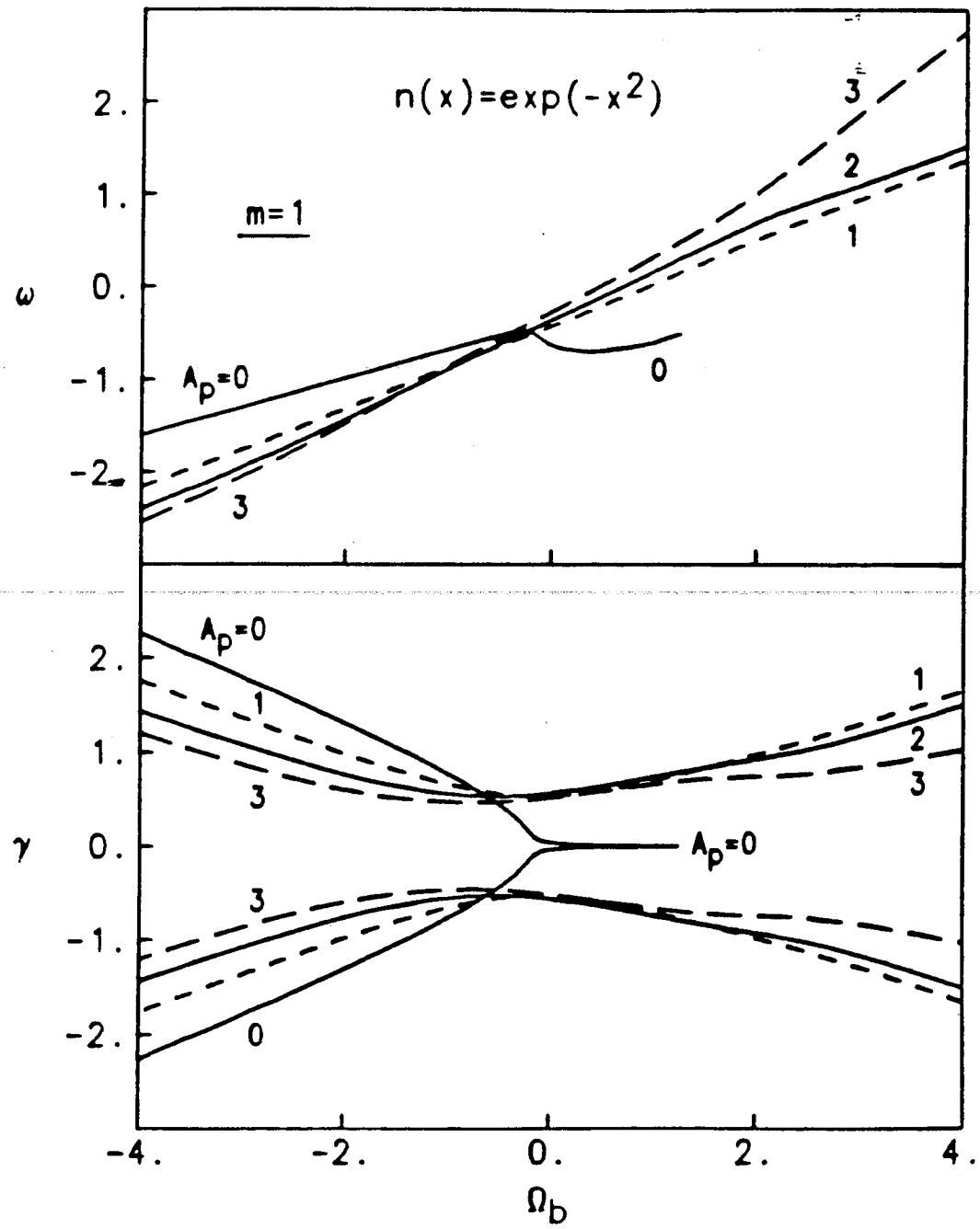

Fig. 11(a)

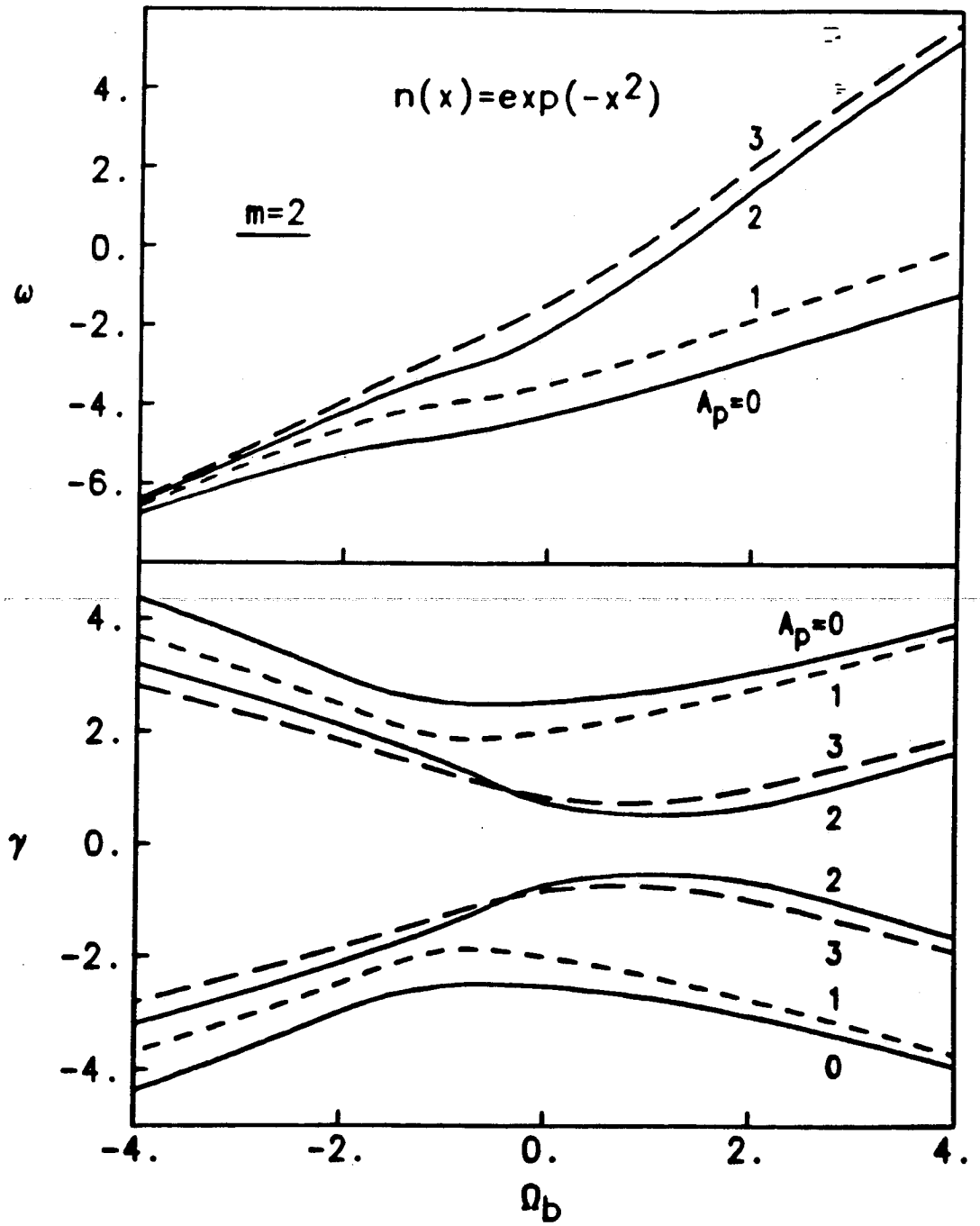

Fig. 11(b)

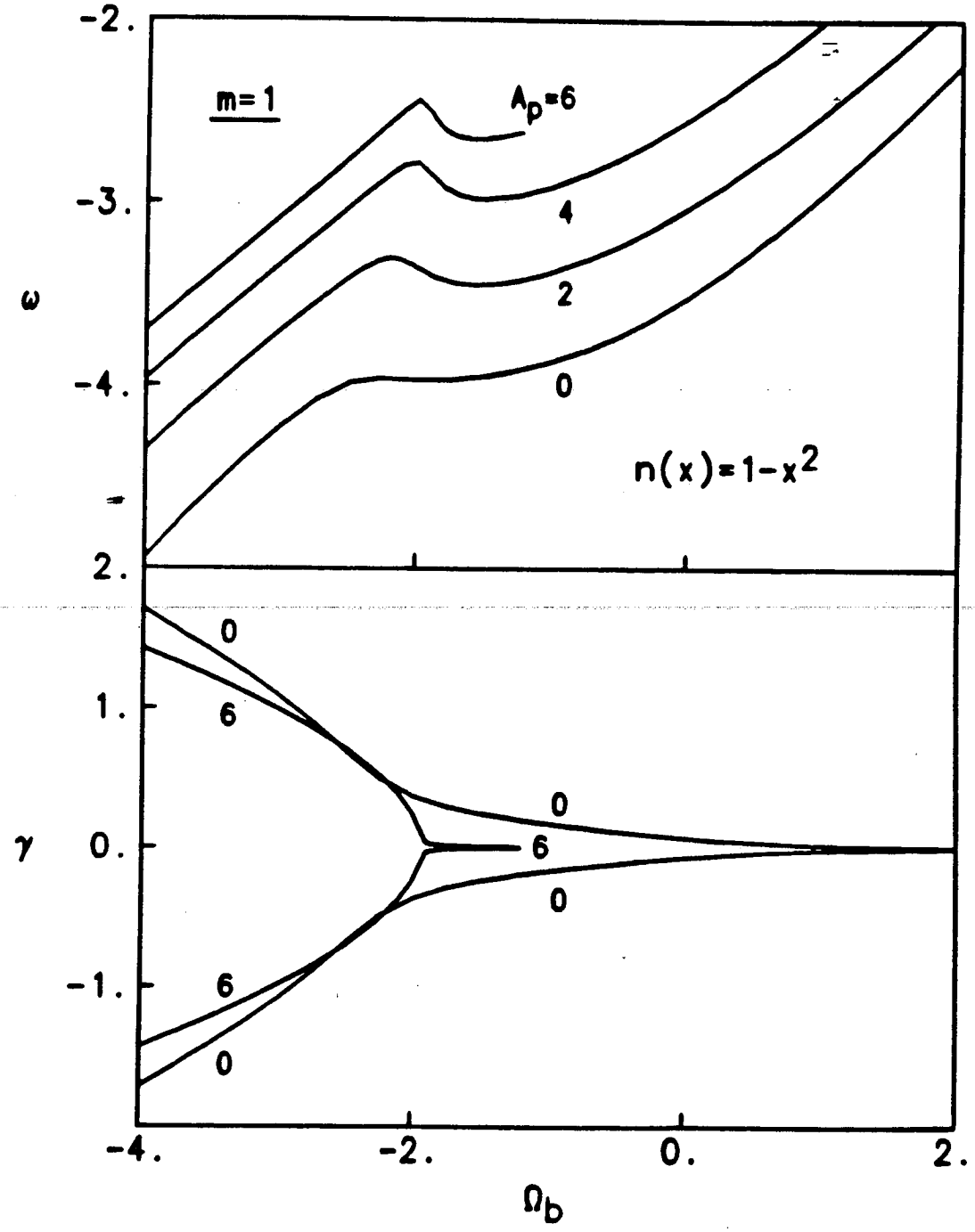

Fig. 12(a)

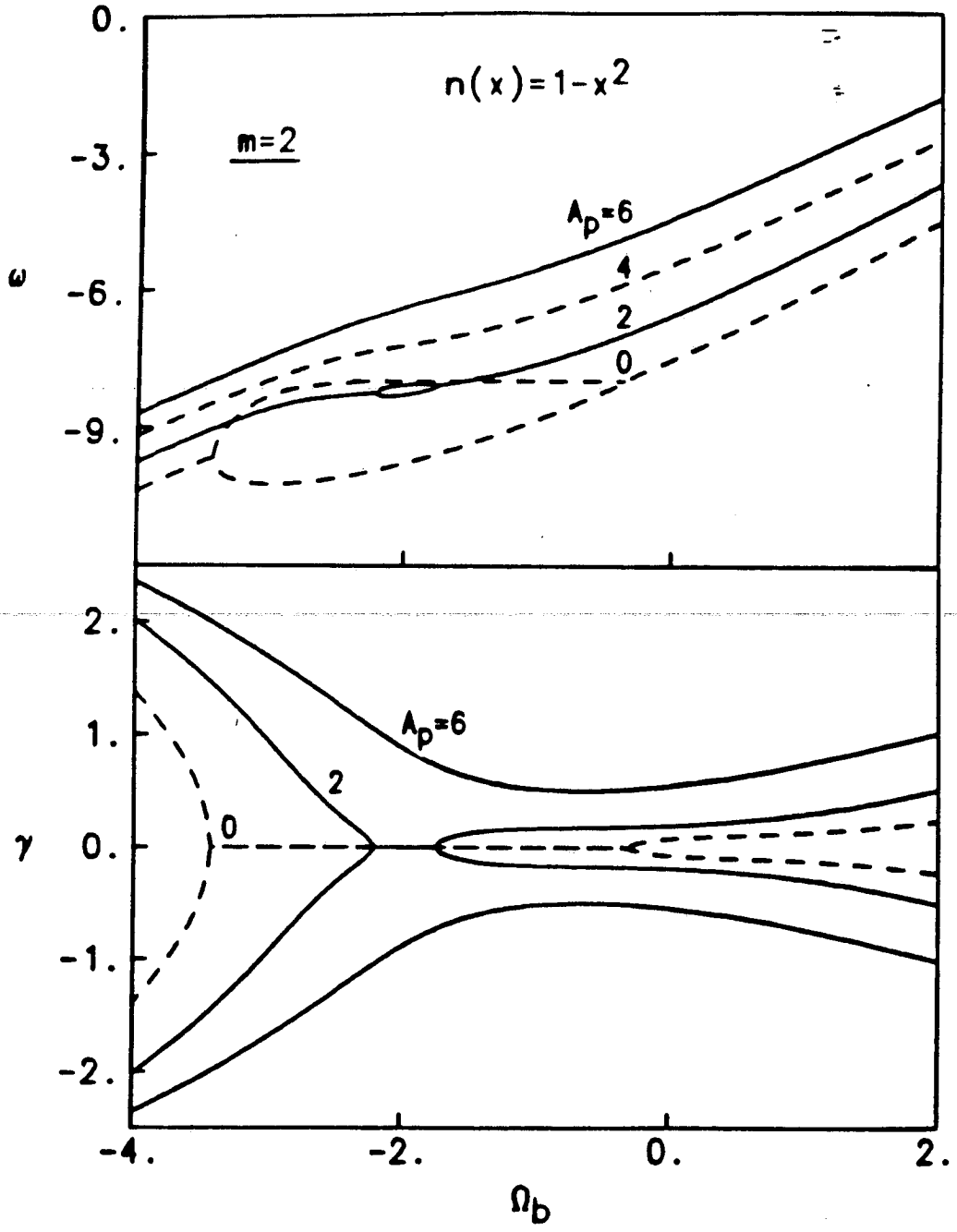

Fig. 12(b)

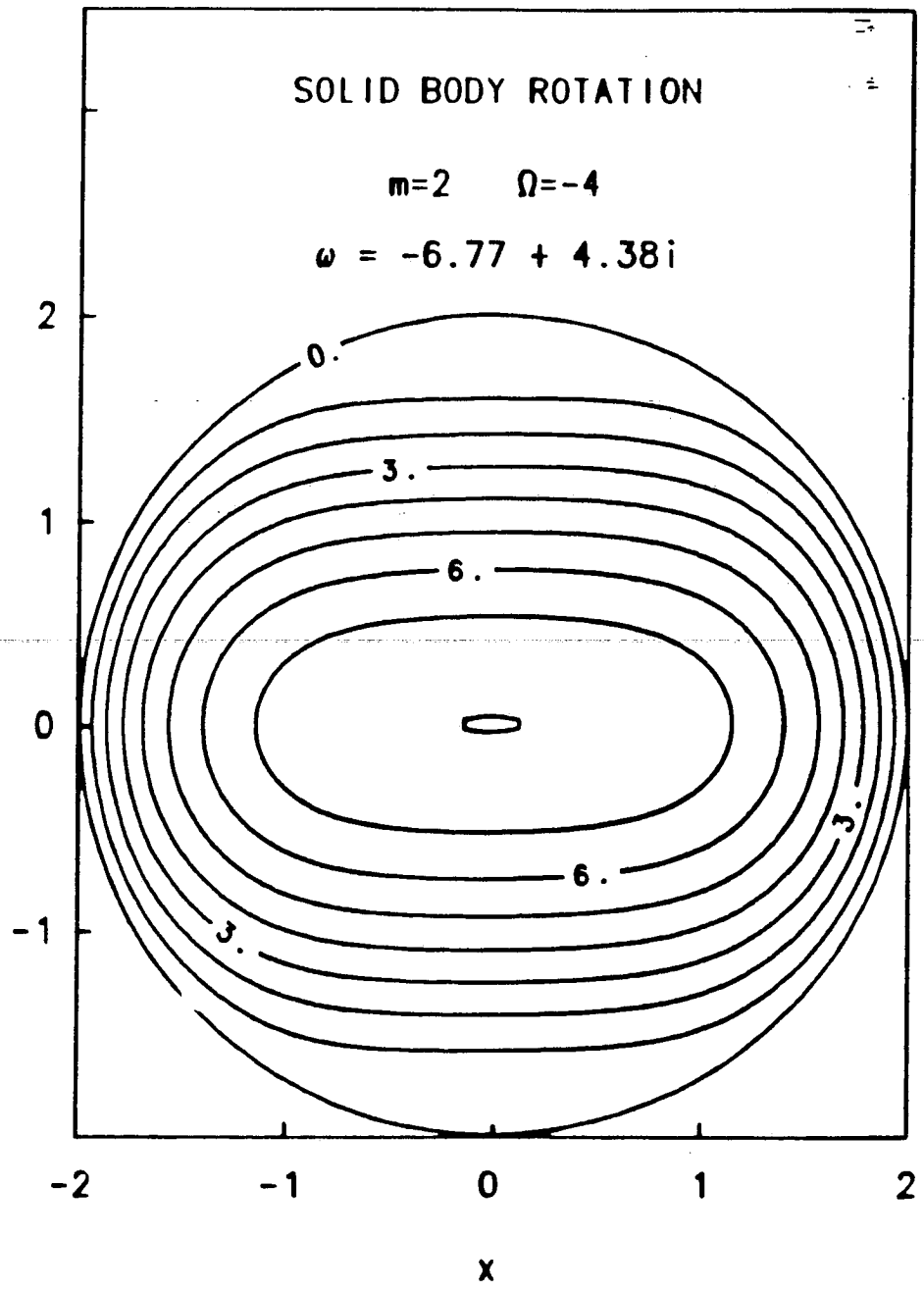

Fig. 13

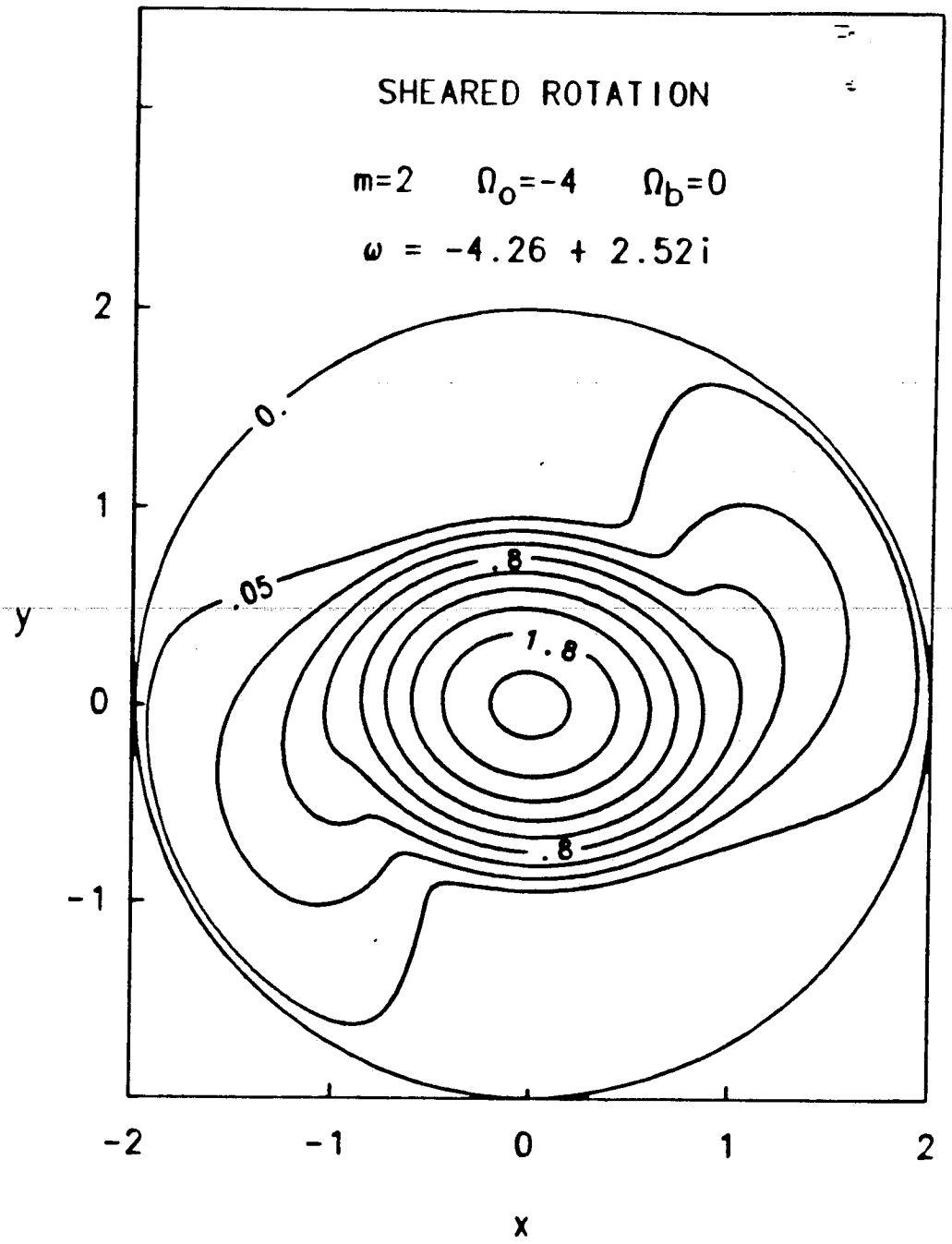

Fig. 14